



## Article

# In Vitro Studies Regarding the Effect of Cellulose Acetate-Based Composite Coatings on the Functional Properties of the Biodegradable Mg3Nd Alloys

Alexandru Streza <sup>1</sup>, Aurora Antoniac <sup>1,\*</sup>, Veronica Manescu (Paltanea) <sup>1,2</sup> , Robert Ciocoiu <sup>1</sup> , Cosmin-Mihai Cotrut <sup>1</sup> , Marian Miculescu <sup>1</sup> , Florin Miculescu <sup>1</sup> , Iulian Antoniac <sup>1,3</sup> , Marco Fosca <sup>4</sup> , Julietta V. Rau <sup>4,5,\*</sup> and Horatiu Dura <sup>6</sup>

<sup>1</sup> Faculty of Material Science and Engineering, National University of Science and Technology Politehnica Bucharest, 313 Splaiul Independentei Street, District 6, 060042 Bucharest, Romania;

alexandru\_streza@yahoo.com (A.S.); veronica.paltanea@upb.ro (V.M.); ciocoiurobert@gmail.com (R.C.); cosmin.cotrut@upb.ro (C.-M.C.); marian.miculescu@upb.ro (M.M.); f\_miculescu@yahoo.com (F.M.); antoniac.iulian@gmail.com (I.A.)

<sup>2</sup> Faculty of Electrical Engineering, National University of Science and Technology Politehnica Bucharest, 313 Splaiul Independentei Street, District 6, 060042 Bucharest, Romania

<sup>3</sup> Academy of Romanian Scientists, 54 Splaiul Independentei Street, District 5, 050094 Bucharest, Romania

<sup>4</sup> Istituto di Struttura della Materia, Consiglio Nazionale delle Ricerche (ISM-CNR), Via del Fosso del Cavaliere 100, 00133 Rome, Italy; marco.fosca@ism.cnr.it

<sup>5</sup> Department of Analytical, Physical and Colloid Chemistry, Institute of Pharmacy, I.M. Sechenov First Moscow State Medical University, Trubetskaya Street 8, Build. 2, 119048 Moscow, Russia

<sup>6</sup> Faculty of Medicine, Lucian Blaga University of Sibiu, 2A Lucian Blaga Street, 550169 Sibiu, Romania; horatiudura@yahoo.com

\* Correspondence: antoniac.aurora@gmail.com (A.A.); giulietta.rau@ism.cnr.it (J.V.R.)

**Abstract:** Magnesium (Mg) alloys are adequate materials for orthopedic and maxilo-facial implants due to their biocompatibility, good mechanical properties closely related to the hard tissues, and processability. Their main drawbacks are the high-speed corrosion process and hydrogen release. In order to improve corrosion and mechanical properties, the Mg matrix can be strengthened through alloying elements with high temperature-dependent solubility materials. Rare earth elements (RE) contribute to mechanical properties and degradation improvement. Another possibility to reduce the corrosion rate of Mg-based alloys was demonstrated to be the different types of coatings (bioceramics, polymers, and composites) applied on their surface. The present investigation is related to the coating of two Mg-based alloys from the system Mg3Nd (Mg-Nd-Y-Zr-Zn) with polymeric-based composite coatings made from cellulose acetate (CA) combined with two fillers, respectively hydroxyapatite (HAp) and Mg particles. The main functions of the coatings are to reduce the biodegradation rate and to modify the surface properties in order to increase osteointegration. Firstly, the microstructural features of the experimental Mg3Nd alloys were revealed by optical microscopy and scanning electron microscopy (SEM) coupled with energy-dispersive spectroscopy. Apart from the surface morphology revealed by SEM, the roughness and wettability of all experimental samples were evaluated. The corrosion behavior of the uncoated and coated samples of both Mg3Nd alloys was investigated by immersion testing and electrochemical testing using Simulated Body Fluid as the medium. The complex in vitro research performed highlights that the composite coating based on CA with HAp particles exhibited the best protective effect for both Mg3Nd alloys.

**Keywords:** magnesium alloys; biodegradable alloys; Mg3Nd alloys; cellulose acetate composite coatings; corrosion; surface



**Citation:** Streza, A.; Antoniac, A.; Manescu, V.; Ciocoiu, R.; Cotrut, C.-M.; Miculescu, M.; Miculescu, F.; Antoniac, I.; Fosca, M.; Rau, J.V.; et al. In Vitro Studies Regarding the Effect of Cellulose Acetate-Based Composite Coatings on the Functional Properties of the Biodegradable Mg3Nd Alloys. *Biomimetics* **2023**, *8*, 526. <https://doi.org/10.3390/biomimetics8070526>

Academic Editor: Xiang Ge

Received: 15 September 2023

Revised: 30 October 2023

Accepted: 1 November 2023

Published: 4 November 2023



**Copyright:** © 2023 by the authors. Licensee MDPI, Basel, Switzerland. This article is an open access article distributed under the terms and conditions of the Creative Commons Attribution (CC BY) license (<https://creativecommons.org/licenses/by/4.0/>).

## 1. Introduction

Recently, magnesium (Mg) alloys have been considered the most adequate materials in the biomedical field because they exhibit high specific strength, are lightweight, and

have good castability, heat dissipation, and machinability [1–3]. It was shown that the magnesium ion release process has a beneficial effect on angiogenesis and osteogenesis, a fact that makes this material adequate for better orthopedic fixation [4–7]. Their main drawback is considered to be the high-speed degradation process, which occurs when the Mg implant is introduced in physiological media, followed by hydrogen evolution [8]. This last-mentioned effect should be carefully controlled by considering its potential to induce necrosis of healthy tissue. Magnesium cannot be combined during implant manufacture with other parts made of such materials as copper (Cu), titanium (Ti), aluminum (Al) alloys, and stainless steel due to galvanic corrosion. It was noticed that high-purity magnesium exhibits the lowest corrosion rate because it contains  $\alpha$ -Mg in the microstructure [9]. The material properties can be controlled and modified in a desired fashion by adding alloying elements, whose selection must be carefully performed by considering the difficulty of Mg alloy manufacturing due to its increased pyrophoricity when it is used as powder.

It is well known that Mg chemically reacts with alloying compounds and generates intermetallic phases with an important influence on the material microstructure. In some cases, the mechanical properties of the alloys can be improved due to precipitation hardening and solid-solution or grain-refinement strengthening phenomena [10]. The Mg matrix can be strengthened through alloying with high temperature-dependent solubility materials [11]. The element's atomic size with respect to Mg and its valence greatly influence the overall solubility. By modifying the alloying element number and weight, alloys with different properties and corrosion behavior can be obtained. An important alloying element with good biocompatibility is Zinc (Zn). The tolerance limit for this element in Mg was established at 2.5 wt.% [12]. The literature evidenced that the corrosion resistance decreased when the Zn content was increased from 1 to 3 wt.% [13]. If it is higher than 3 wt.%, stress corrosion cracks occur. The Zn percent must be carefully checked because it acts in the biocorrosion process by decreasing the hydrogen evolution. Zn is highly biocompatible, being present in the human body in bones and muscles. Due to its higher Young modulus compared to that of Mg, a non-uniform load transfer between the implant and bone tissue was observed [14]. Zirconium (Zr) is used for grain refinement, although the literature shows that it promotes anode chemical reactions and can damage the surface coatings. Its quantity must be tuned in order to have reduced corrosion rates.

Rare earths (RE) contribute to mechanical property improvement, altering the material texture and influencing the degradation behavior. In [15,16], it was observed that RE addition facilitates the enhanced performance of Mg alloys when they work at high temperatures. The most used REs as alloying elements in Mg-based alloys are cerium (Ce), neodymium (Nd), yttrium (Y), gadolinium (Gd), lanthanum (La), and praseodymium (Pr). RE forms a stable ternary eutectic compound Mg-Zn-RE, which improves the creep resistance and castability of Mg-Zn-Zr alloy [17]. Loos et al. [18] investigated the Y biocompatibility based on in vitro and in vivo tests on Mg stents. They found that accumulation in the gallbladder and liver is possible if a high Y concentration is used. Also, Y caused increased eosinocyte levels in the blood and has a detrimental effect on implant biocompatibility. Other studies showed that the amount of added Nd must be controlled because the formation of the Mg<sub>3</sub>Nd phase in the binary alloy Mg-Nd increases its corrosion rate. As an overall finding, its corrosion rate is much more reduced in comparison with that obtained through La or Ce addition [1]. Nd determines the appearance of a shielded oxide layer at the surface of Mg alloys. Another RE with a positive impact on corrosion resistance is Gd because, by its addition, a high solid solution in Mg occurs. It was noticed that Gd provides good corrosion resistance only if its content is lower than 10 wt.% [19]. Due to its toxicity in the case of medical implants, it can be added only in an amount lower than 1 wt.% [20]. Cerium decreased the corrosion rate in the case of Mg-Zn-Zr and Mg-Al-Zn alloys by reducing the grain size [21]. Unfortunately, in vivo studies performed on murine animal models show evidence that Ce disturbed the function of the liver, brain, and kidneys. It is well known that an increase in the metallothioneins (MTs) induced by heavy metal exposure can offer protection against oxidative stress. At the same time, glutathione

(GSH) is another antioxidant that plays an important role in cellular defense. In [22], an increase in GSH and MT concentration was evidenced for cerium-treated ICR mice. The authors concluded that Ce could be considered oxidant toxic for mice because it generated hepatic MT synthesis, decreased hepatic Lipoperoxide concentration, and increased hepatic GSH concentration, among others. Willbold et al. [23] investigated the biocompatibility of the following binary alloys: Mg-La, Mg-Nd, and Mg-Ce. They observed that these alloys showed no toxicity against the healthy tissue, although the Mg-Ce exhibited the most reduced cell viability. In conclusion, the authors stated that RE addition improves the corrosion rate and mechanical properties, but their content should be carefully tuned in order to avoid unwanted biological effects. He et al. [24] investigated the effect of Zn addition on the mechanical properties and microstructure of the Mg-3Y-2Nd-0.5Zr alloy. They added 0.5 wt.% Zn and applied a solid solution treatment at 525 °C and an aging step at 200 °C. Zn-Zr precipitates with a rod-like and rectangular block-like shape were noticed in the  $\alpha$ -Mg matrix, and many needle-like  $\beta$  phases were present at the terminal parts of Zn-Zr precipitates in the case of samples, for which an aging treatment was applied. Chen et al. [25] modified the Y concentration (0, 0.03, 0.06, 0.12 at.%) in the Mg-Nd-Zn-Zr alloy. A phase consisting of Mg<sub>24</sub>Y<sub>5</sub> appeared in the case of Y-containing alloys. Supplementary, a grain-refining process was put in evidence. The UTS value increased directly with the Y content from 300 MPa (0 at.%) to 320 MPa (0.12 at.%).

The insight gained herein may help equip practitioners with an understanding of the structure–property relationship, towards rational material selection and manipulation [26].

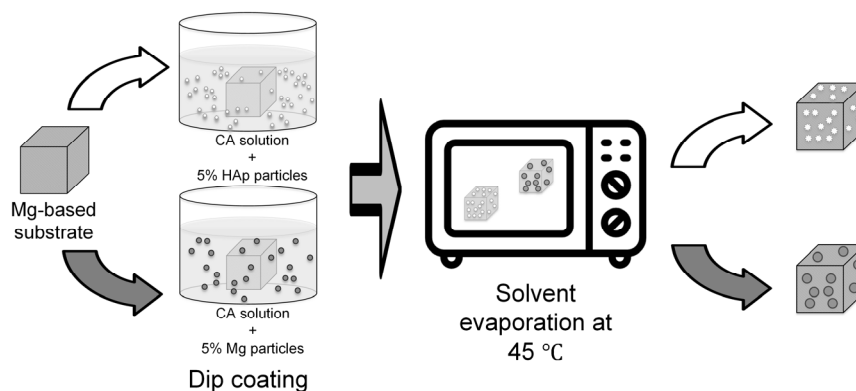
Kirkland et al. [27] conducted a survey on the bio-corrosion rates of magnesium alloys. They analyzed the dissolution rates and mass loss of different Mg alloys using Minimum Essential Medium (MEM) incubated at 37 °C in 5.0% CO<sub>2</sub>. In the case of the Mg1Nd alloy, all the mass loss values measured at 3, 7, and 14 days were below 1 mg/cm<sup>2</sup>/day. Other Mg-RE alloys exhibited an increased mass loss, such as Mg1Ce with a mass loss of about 1 mg/cm<sup>2</sup>/day and Mg0.5Y with a value of 2 mg/cm<sup>2</sup>/day. The highest mass loss was obtained for the Mg5Ca alloy with a value higher than 10 mg/cm<sup>2</sup>/day, measured after 3 days of immersion. It can be concluded that RE addition has a beneficial effect on increasing corrosion resistance.

The degradation rate of Mg-based alloys can be reduced through coating deposition. Different coatings, such as bioceramic, polymeric, and polymeric-based composites, are reported in the literature as having a positive effect on different magnesium-based alloy biodegradations [28–35]. Polymeric coatings can be of natural or synthetic origins and can be used to deliver different drugs or treatments. Some of the most common synthetic polymers are cellulose acetate (CA), polylactic acid (PLA), polycaprolactone (PCL), and poly(lactide-co-glycolic) acid (PLGA), and they can be combined with calcium phosphate (Ca-P) or Mg powders in order to improve the corrosion and wear resistance of the alloy [31]. Cellulose acetate is a biocompatible, non-toxic polymer that forms transparent films. Membranes manufactured from this polymer are characterized by a hydrophilic nature, chemical stability, good mechanical properties, reduced protein adsorption, and protein transport capabilities. Neacsu et al. [32] applied a CA coating on the Mg-Ca-Mn-Zr alloy through a dipping process. The potentiodynamic polarization investigation proved that this coating increased the corrosion resistance of the alloy. Supplementary, good cytocompatibility on the MC3T3-E1 cell line was noticed. It was concluded that even though only a few studies were reported in the literature, CA exhibits high biocompatibility and can be used in safe conditions as a coating for scaffolds or implants. Various groups have proposed other synthetic polymers to be used as coatings for degradable Mg alloys, as presented in Table 1.

**Table 1.** Synthetic polymer coatings applied on Mg-based alloys.

Coating	Mg-Based Substrate	Remarks	Ref
PLA	Mg9Al1Zn	The authors investigated the degradation of samples in simulated body fluid (SBF) based on electrochemical impedance spectroscopy (EIS). It was concluded that a thickness of 5 $\mu\text{m}$ for the polymeric coatings determines a corrosion resistance increase of two times compared to the bare Mg alloy. Thicker PLA layers were linked to poor adhesion.	Alabbasi et al. [33]
PLA/micro-arc oxidation (MAO)	Mg3Al1Zn	After the MAO process was applied, a 5 $\mu\text{m}$ porous MgO layer was obtained. Then, the samples were immersed in PLA, and a coating with 9 $\mu\text{m}$ thickness was formed. Following the electrochemical corrosion analysis in the case of coated samples, the corrosion potential was about $-1.51\text{ V}$ , and the corrosion current density had a very low value, equal to $1.83\ \mu\text{A}/\text{cm}^2$ .	Shi et al. [34]
PCL (3% (w/v)) and PCL (6% (w/v))	Mg-based scaffolds	It was noticed that the uncoated scaffolds fully degraded after 72 h, and the coated samples degraded in a proportion of 36% and 23%.	Yazdimamaghani et al. [35]
PLGA	Mg6Zn	PLGA was dissolved in chloroform with 2 wt.% and 4 wt.% concentrations. The corrosion analysis revealed a very low value for the corrosion current density in the coated samples compared to the control one.	Li et al. [36]
(MAO) + PLGA	Mg4Zn0.6Zr0.4Sr	Compared with the uncoated sample, the (MAO) + PLGA coatings increased the corrosion resistance of the alloy by three orders of magnitude, and the stress corrosion cracking susceptibility measurements were reduced by 75% of the ultimate tensile strength.	Chen et al. [37]
Composite coatings based on CA, CA-HAp, CA-Mg, and CA-HAp-Mg	-	They noticed that the thermogravimetric analysis proved the coating stability up to 200 $^{\circ}\text{C}$ , highlighting a mass loss with a maximum value of 9% at a maximum temperature of 250 $^{\circ}\text{C}$ . HAp crystals were put in evidence through scanning electron microscopy investigations. The CA-Mg and CA-HAp composite coatings were characterized by a viability of 80% for the MG-63 cell line.	Streza et al. [38]

The present investigation consists of polymeric-based composite coatings made of CA combined with two bioactive fillers, such as HAp or Mg particles, applied on the surface of two Mg3Nd alloys to reduce the biodegradation rate and to increase the surface osteointegration (Figure 1).

**Figure 1.** Schematic diagram of the preparation method for the coated Mg-based samples.

## 2. Materials and Methods

In this study, two experimental magnesium alloys from the system Mg3Nd, with Y, Zr, and Zn as other alloying elements (Mg-Nd-Y-Zr-Zn), with elemental compositions given in Table 2, were selected to be characterized and tested to evaluate their potential as raw materials for trauma implant fabrication. The alloys were obtained by sand/gravity casting, as described previously [38,39].

**Table 2.** Elemental composition of the Mg3Nd alloys.

Alloys	Composition (wt.%)				
	Zn	Zr	Y	Nd	Mg
Mg3Nd_A	0.3	0.6	2.10	3.2	Bal
Mg3Nd_B	0.3	0.4	0.21	3.1	Bal

To reduce the rapid degradation in physiological environments with a pH between 7.4 and 7.6, the investigated alloys were coated using a CA solution with HAp (Sigma-Aldrich, St. Louis, MO, USA) or Mg (STREM CHEMICALS Inc., USA) particles. The polymer solution (at a concentration of 12 wt.%) was obtained under vigorous mechanical stirring by dissolving CA (Sigma-Aldrich, St. Louis, MO, USA—30% acetylation degree) in N,N'-dimethylformamide (Merck, Darmstadt, Germany). The HAp and Mg particles were dispersed in the polymer solution in a proportion of 5 wt.% related to the amount of cellulose acetate. For the Mg3Nd alloy coating, samples with dimensions of 15 × 15 × 5 mm<sup>3</sup> were immersed in the obtained polymer solution, followed by evaporation of the solvent for 3 days at a temperature of 45 °C. The operation was repeated three times to obtain a homogeneous coating. After the coating process, the samples were coded as follows: *Mg3Nd\_A\_CAHAp*–Mg3Nd\_A alloy with a composite coating based on CA reinforced with HAp, *Mg3Nd\_A\_CAMg*–Mg3Nd\_A alloy with a composite coating based on CA reinforced with Mg, *Mg3Nd\_B\_CAHAp*–Mg3Nd\_B alloy with a composite coating based on CA reinforced with HAp, and *Mg3Nd\_B\_CAMg*–Mg3Nd\_B alloy with a composite coating based on CA reinforced with Mg. Before characterization and testing, the uncoated and coated alloys were washed with ethanol (Sigma-Aldrich, St. Louis, MO, USA).

### 2.1. Materials Characterization

The Mg3Nd alloys' microstructure was evaluated using an Olympus BX51 optical microscope (Olympus Life and Materials Science Europa GMBH, Hamburg, Germany) and an FEI QUANTA INSPECT F microscope (FEI Company, Eindhoven, The Netherlands) equipped with an EDS analyzer. For microstructural analysis, the metallographically prepared magnesium alloy samples were chemically etched with a solution of 2.4 g of picric acid, 18 mL of glacial acetic acid, 76 mL of ethanol, and 18 mL of distilled water. Also, the surface morphology of the coated Mg3Nd alloys and the layer thickness were highlighted using scanning electron microscopy (SEM).

### 2.2. Corrosion Behavior of the Experimental Samples

#### 2.2.1. Immersion Test

To evaluate the mass loss, we used five cuboid samples from each type of uncoated and coated alloy with dimensions of 15 × 15 × 5 mm<sup>3</sup> (length × width × thickness). The test was carried out at 37 ± 1 °C for 72, 168, and 336 h, each sample being introduced into 50 mL of test medium. We used Kokubo's simulated body fluid solution (SBF, prepared in our laboratory according to [40]) as a test medium. The solution was changed daily to simulate the human body's environment as accurately as possible.

The mass loss was calculated using the following equation:

$$ML = \frac{m_0 - m_f}{m_0} \times 100 \quad (1)$$

where  $ML$ —the mass loss (%),  $m_0$ —initial mass value, and  $m_f$ —final mass value.

### 2.2.2. Electrochemical Tests

The corrosion behavior of the two Mg3Nd alloys was investigated with a PARSTAT 4000 Potentiostat/Galvanostat device (Princeton Applied Research, Oak Ridge, TN, USA) in SBF solution (pH of 7.4), following the ASTM G5-94 (2011) standard at  $37 \pm 0.5$  °C in a CW-05G (Jeio Tech) recirculation and heating bath. A three-electrode cell comprised of a counter electrode consisting of a platinum foil, a saturated calomel electrode, SCE, and the sample as a working electrode was involved.

The corrosion potential ( $E_{corr}$ ) and corrosion current density ( $i_{corr}$ ) were extrapolated from the Tafel curves that were experimentally measured in the condition of an applied potential range of  $\pm 250$  mV vs. EOC (potential rich at quasi-equilibrium) at a speed of 1 mV/s. The EOC was measured for one hour until the system reached a quasi-equilibrium state. The polarization resistance  $R_p$  ( $k\Omega cm^2$ ) was determined as indicated in ASTM G59-97 according to Equation (2):

$$R_p = \frac{1}{2.3} \frac{\beta_a \beta_c}{\beta_a + \beta_c} \frac{1}{i_{corr}} \quad (2)$$

$\beta_a$  (mV)—the slope of the Tafel anodic curve,  $\beta_c$  (mV)—the slope of the Tafel cathodic curve.

The corrosion rate was computed as presented in Equation (3) and ASTM G102-89 for uncoated samples:

$$CR = K_i \frac{i_{corr}}{\rho} EW \quad (3)$$

$CR$ —the corrosion rate (mm/year),  $K_i = 3.27 \times 10^{-3}$  ( $C^{-1}$ ),  $i_{corr}$ —the corrosion current density ( $\mu A/cm^2$ ),  $\rho$ —the material density ( $g/cm^3$ ), and  $EW$ —the equivalent weight (g).

Another important parameter, which can be determined only in the case of coated samples, is the protective efficiency (Equation (4)):

$$P_e = \left( 1 - \frac{i_{corr,coating}}{i_{corr,substrate}} \right) 100 \quad (4)$$

$i_{corr,coating}$  ( $\mu A/cm^2$ )—the corrosion current density for the Mg3Nd alloy coatings and  $i_{corr,substrate}$  ( $\mu A/cm^2$ )—the corrosion current density for the Mg3Nd alloys (substrate).

### 2.3. Surface Properties of the Experimental Samples

The equipment involved in the material *wettability investigations* was the Krüss Drop Shape Analyzer-DSA100 (A. Krüss Optronic GmbH, Hamburg, Germany). This device is suitable for experiments with three wetting agents: water (W), diiodomethane (DIM), and ethylene glycol (EG). All the measurements were performed in laboratory conditions ( $23 \pm 5$  °C, humidity of  $45 \pm 5\%$ ). We analyzed six samples for both Mg3Nd alloys (two control samples, two samples coated with composite coatings based on CA and 5% HAP particles, and two samples coated with composite coatings based on CA and 5% Mg particles). For each wetting agent, 12 successive measurements were performed, and the obtained images were analyzed based on ImageJ 1.50 software (National Institutes of Health, Bethesda, MD, USA). The Owens, Wendt, Rabel, and Kaelbe (OWKR) procedure was applied to compute the surface free energy (SFE) [41].

The profilometry analysis was made with a Form Talysurf® I-Series PRO Range Taylor Hobson Ametek (Warrenville, IL, USA) device and measures *roughness* according to ISO 21920. It uses Metrology 4.0 Software (Taylor Hobson Ametek, IL, USA) and has a transducer with a standard probe.

Based on five observations, we determine the  $R_a$  (arithmetic average deviation from the mean line) and  $R_q$  (root mean square average of the profile heights over the evaluation length) parameters.

### 3. Results and Discussion

#### 3.1. Microstructural Characterization of the Alloys

Figures 2–5 show the optical micrographs corresponding to Mg3Nd\_A and Mg3Nd\_B alloys before and after metallographic etching at different magnifications.

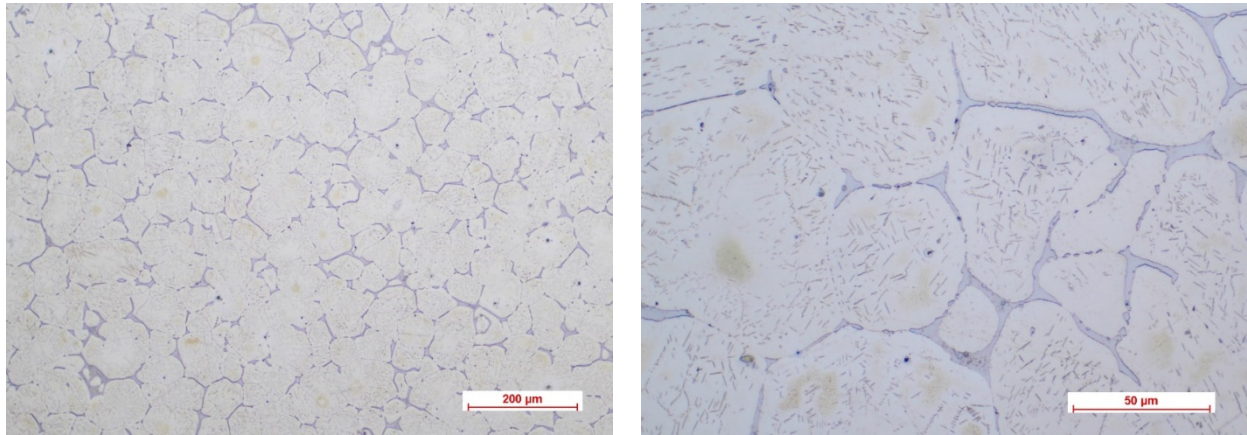


**Figure 2.** The optical micrographs corresponding to the Mg3Nd\_A alloy (10× and 50×).

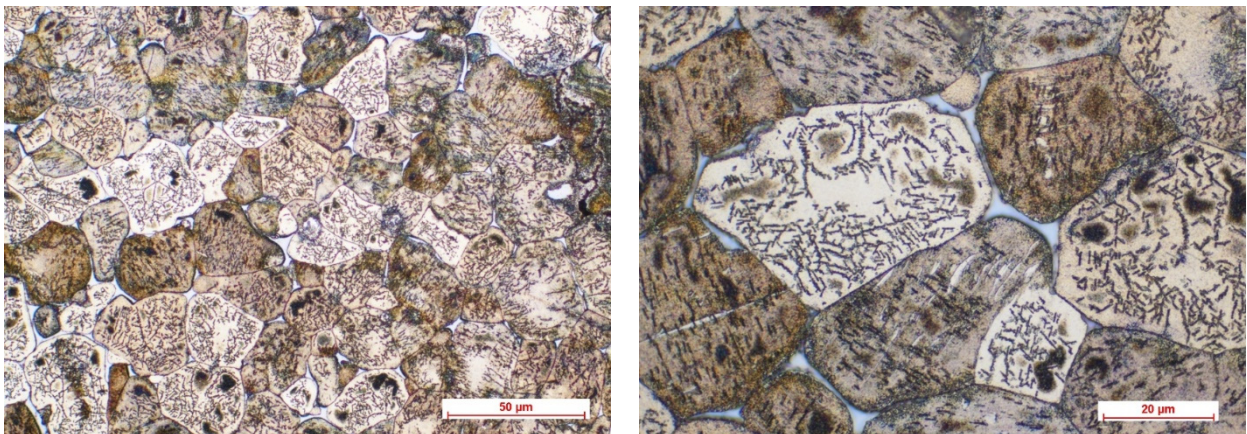


**Figure 3.** The optical micrographs corresponding to the Mg3Nd\_A alloy (50× and 100×) after metallographic etching.

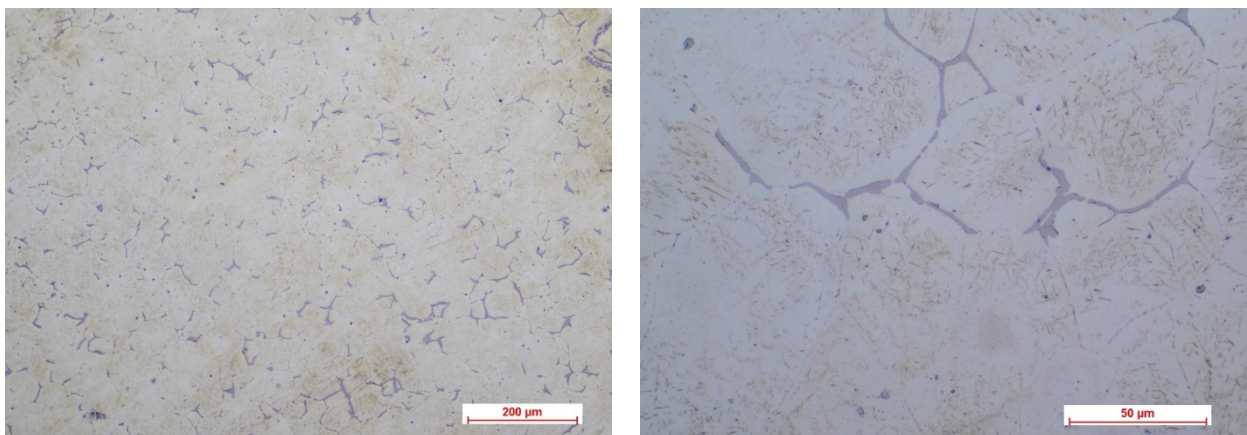


**Figure 4.** The optical micrographs corresponding to the Mg3Nd\_B alloy (10× and 50×).

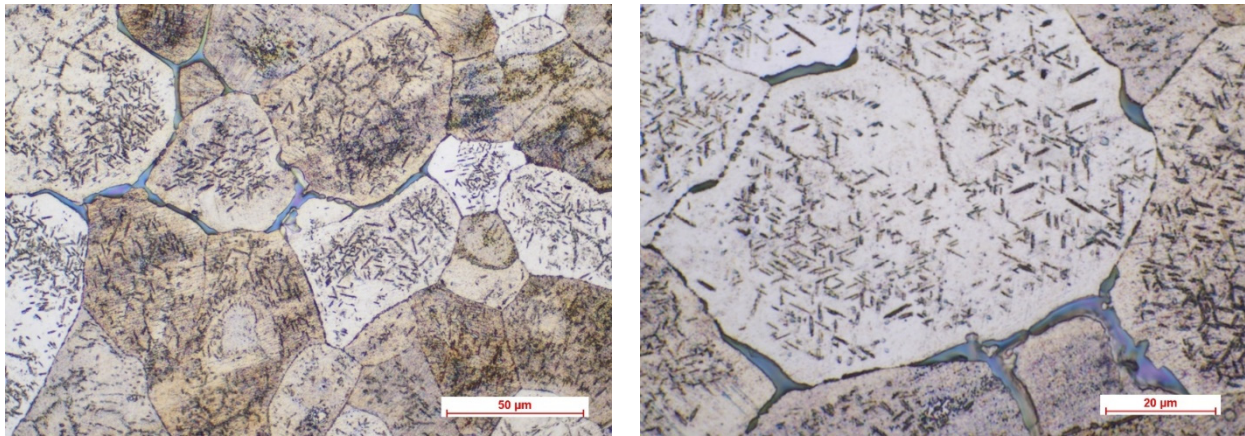


**Figure 5.** The optical micrographs corresponding to the Mg3Nd\_B alloy (50× and 100×) after metallographic etching.

The alloys' microstructure is formed by uniform polyhedral grains of  $\alpha$ -Mg, in which secondary phases are precipitated, with different morphologies, from acicular to globular, uniformly distributed in the  $\alpha$ -Mg grains. The micrographs also highlight a distinct phase at the grain boundary, most likely a multicomponent intermetallic compound. In the Mg3Nd\_A alloy, compared to the Mg3Nd\_B alloy, the grains are smaller and more uniform in size, the degree of intragranular precipitation is higher, and acicular (icosahedral) compounds are the majority, tending to group "in packages" which will assure better mechanical properties for these alloys. The effect of the presence of a larger amount of Y in the chemical composition of the Mg3Nd\_A alloy, as well as of Nd, materializes through the uniformity of the grain size, simultaneously with its reduction. Also, the proportion of the phase at the grain boundaries is visibly reduced in the Mg3Nd\_B alloy, becoming insular, which will increase the alloy's ductility.

Other studies found similar results regarding the Y and Nd effects on the alloy microstructure. Xu et al. [42] prepared through the extrusion technique the Mg-Zn-Y-Zr alloy. They varied the yttrium composition between 0 and 3.5 wt.%, proving that Y addition has a grain refinement effect and increased mechanical strength by forming the I-phase ( $\text{Mg}_3\text{YZn}_6$ ) in the Mg matrix. At a concentration higher than 1.72 wt.%, the mechanical strength decreased due to the appearance of the W-phase ( $\text{Mg}_3\text{Y}_2\text{Zn}_3$ ). It was concluded that the best mechanical properties were achieved for a Y proportion between 1.17 and 1.72 wt.%. Wang et al. [43] investigated the influence of Nd content on the microstructure of  $\text{Mg}_{4.5}\text{Zn}_1\text{Y}_x\text{Nd}_{0.5}\text{Zr}$  ( $x = 0, 1 \text{ wt.}\%, 2 \text{ wt.}\%, 3 \text{ wt.}\%$ ). Optical microscopy revealed that in the case of 0 wt.% alloy, the main phases are  $\alpha$ -Mg,  $\text{Mg}_3\text{Y}_2\text{Zn}_3$  (W), Zn-Zr, and  $\text{Mg}_3\text{YZn}_6$  (I). When Nd was added, the I-phase was not observed anymore, and  $\text{Mg}_3\text{Y}_2\text{Zn}_3$  changed to  $\text{Mg}_3(\text{Nd}, \text{Y})_2\text{Zn}_3$ . It was observed that at 3 wt.% Nd a ternary phase of Mg-Zn-Nd occurred, concomitantly to an increase in intermetallic phases and a reduction in secondary dendritic arm spacing. Zhou et al. [44] performed an investigation regarding the effect of Y and Nd addition to the  $\text{Mg}_6\text{Zn}_{0.6}\text{Zr}$  (ZK60) alloy. They observed two new phases,  $\text{Mg}_3\text{Zn}_6\text{Y}$  (I-phase) and  $\text{Mg}_{41}\text{Nd}_5$ , grain refinement, and improved mechanical properties. Zengin and Turen [45] analyzed the effect of Y addition on the microstructure of  $\text{Mg}_6\text{Zn}_{0.5}\text{Zr}_1\text{Nd}_x\text{Y}$  ( $x = 0, 0.5, 1, 2$ ). They noticed that the as-cast microstructure obtained for  $x = 0$  contained  $\alpha$ -Mg and also Mg-Zn-Nd and Mg-Zn phases. With the Y addition appeared two ternary phases, W-phase ( $\text{Mg}_3\text{Zn}_3\text{Y}_2$ ) and I-phase ( $\text{Mg}_3\text{Zn}_6\text{Y}$ ), associated with the grain refinement process.

Figures 6–9 reveal the SEM images and EDS analysis of the Mg3Nd\_A and Mg3Nd\_B alloys at different magnifications. Results sustain the optical investigation, highlighting the morphology and distribution of secondary phases.

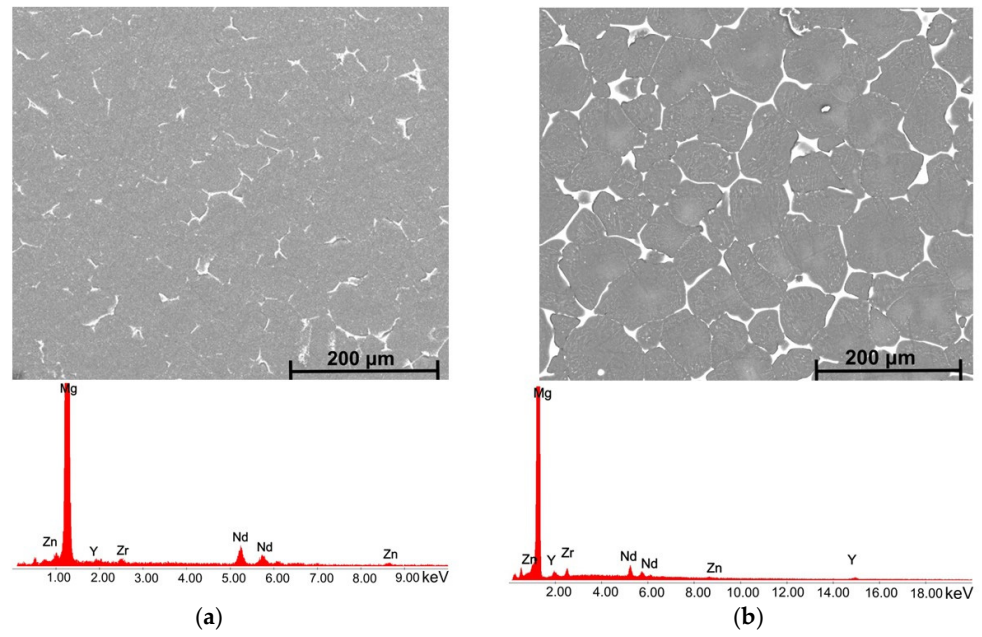


Figure 6. SEM images and EDS spectra for (a) Mg<sub>3</sub>Nd<sub>B</sub> alloy; (b) Mg<sub>3</sub>Nd<sub>A</sub> alloy.

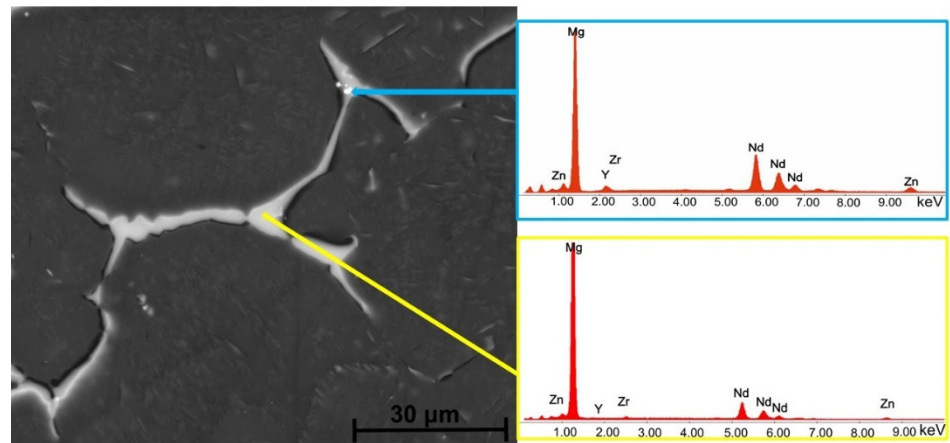


Figure 7. SEM image and associated EDS spectra for Mg<sub>3</sub>Nd<sub>A</sub> alloy.

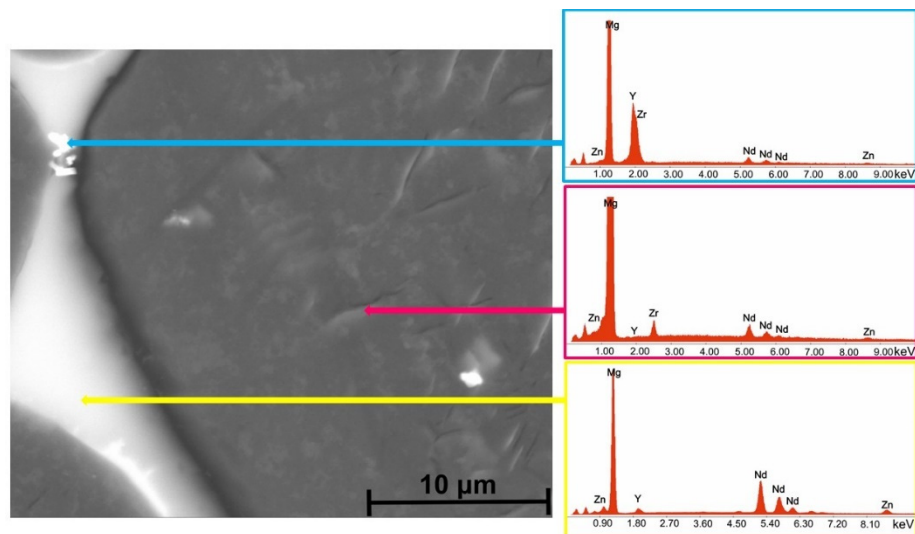
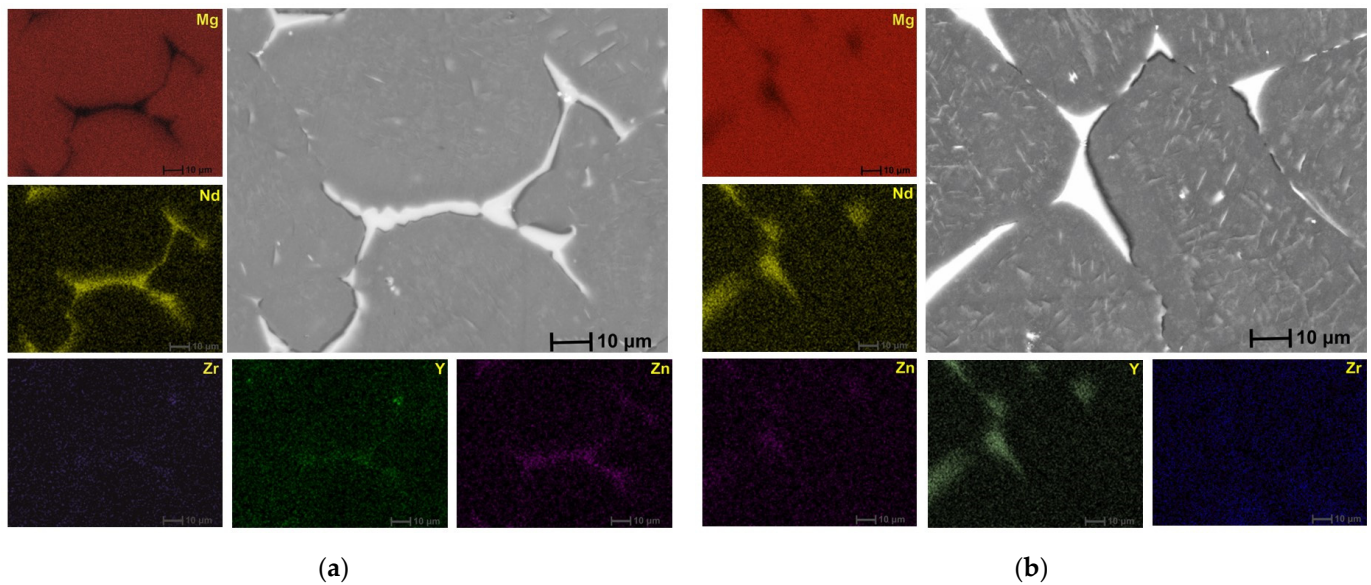


Figure 8. SEM image and associated EDS spectra for Mg<sub>3</sub>Nd<sub>B</sub> alloy.



**Figure 9.** EDS elemental mapping results on (a) Mg<sub>3</sub>Nd\_A alloy; (b) Mg<sub>3</sub>Nd\_B alloy.

According to the EDS results for the Mg<sub>3</sub>Nd\_B alloy, the phase identified at the grain boundary proved to be rich in Mg, Zn, and Nd. Increasing the amount of Y in the alloy composition (Mg<sub>3</sub>Nd\_A alloy), the formation of a grain boundary rich in Mg, Zn, Nd, and Y is observed. Elkaimy et al. [46] and Zengin et al. [45] proposed that the phase be identified as Mg<sub>3</sub>(Nd, Y)<sub>2</sub>Zn<sub>3</sub>. Moreover, the granular compounds present in the alloy structure contain rare earths (Y and Nd), while the acicular compounds are composed of Zr and Zn. Li et al. [47] added Nd and Y to an as-cast Mg<sub>5</sub>Zn<sub>0.6</sub>Zr alloy, and α-Mg phase and compounds such as Mg<sub>4</sub>Zn<sub>7</sub> and Zn<sub>2</sub>Zr<sub>3</sub> were observed. Also, a refined microstructure with an increase in the secondary phase was put in evidence.

The surface morphology of the coated Mg<sub>3</sub>Nd alloys and the coating thickness are presented in Figures 10 and 11.

From the SEM images, we can observe that in both cases, the polymeric composite coatings with Mg or HAp particles exhibit a uniform aspect that evidences a homogenous distribution of the particles in the polymeric matrix. Pores with different distributions and average sizes were formed due to the N,N'-dimethylformamide evaporation process, whose particles diffused outside the sample surface. The main conclusion that can be extracted is that the developed coatings are very well prepared, and in the case of composite coating with Mg particles, a much smoother surface is evidenced. The cross-section images underline the abovementioned findings and show that both coatings are homogeneously placed on the Mg<sub>3</sub>Nd alloy surface. We determined, for the coating thickness in the case of Mg<sub>3</sub>Nd\_A alloy, values of 42.8 µm (Mg<sub>3</sub>Nd\_A\_CAHAp) and 52.5 µm (Mg<sub>3</sub>Nd\_A\_CAMg).

For the other alloy (Mg<sub>3</sub>Nd\_B), the coating thickness was about 40.9 µm (Mg<sub>3</sub>Nd\_B\_CAHAp) and 53.5 µm (Mg<sub>3</sub>Nd\_B\_CAMg). Due to the different particle natures and interaction forces between CA and the reinforcing agent, the coating thickness exhibits lower values in the case of composite coating with HAp particles.

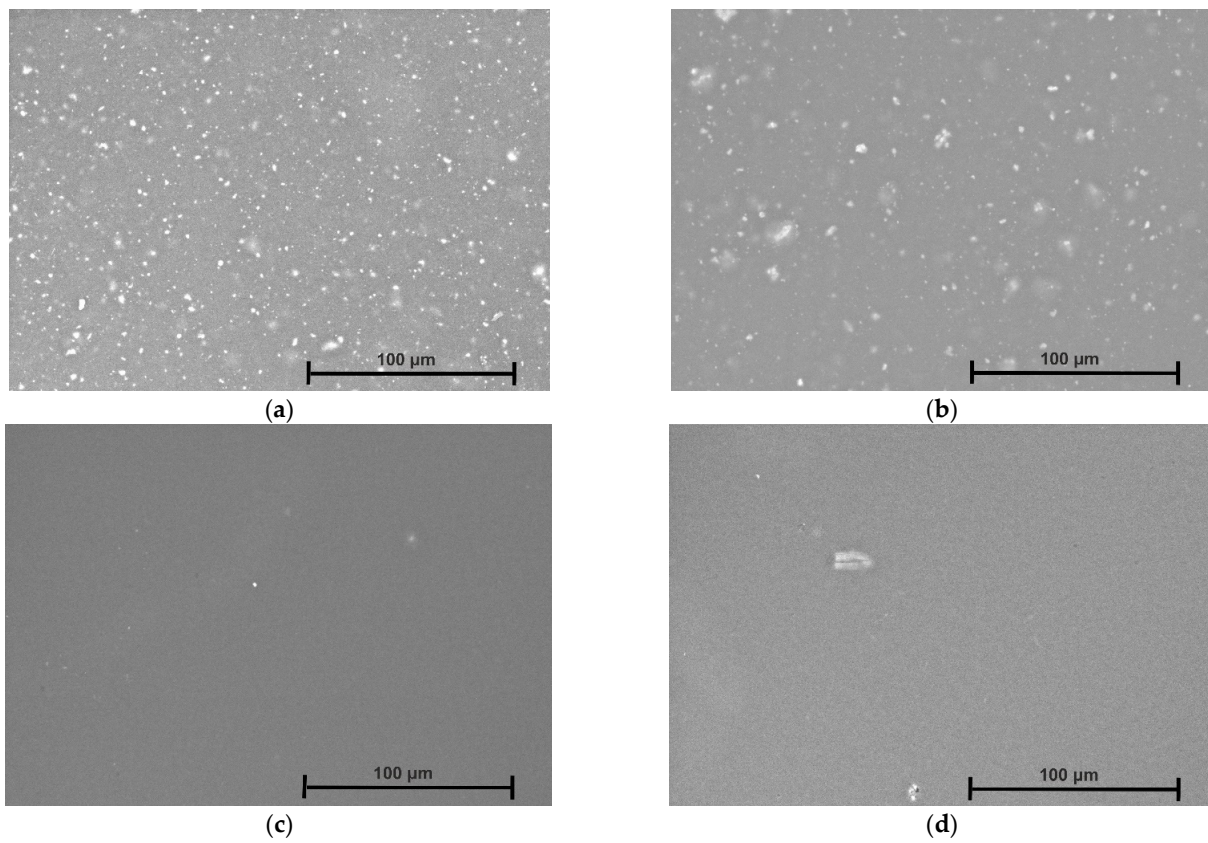


**Figure 10.** SEM images of the coated Mg3Nd alloys: (a) Mg3Nd\_A\_CAHAp; (b) Mg3Nd\_A\_CAMg; (c) Mg3Nd\_B\_CAHAp; (d) Mg3Nd\_B\_CAMg.

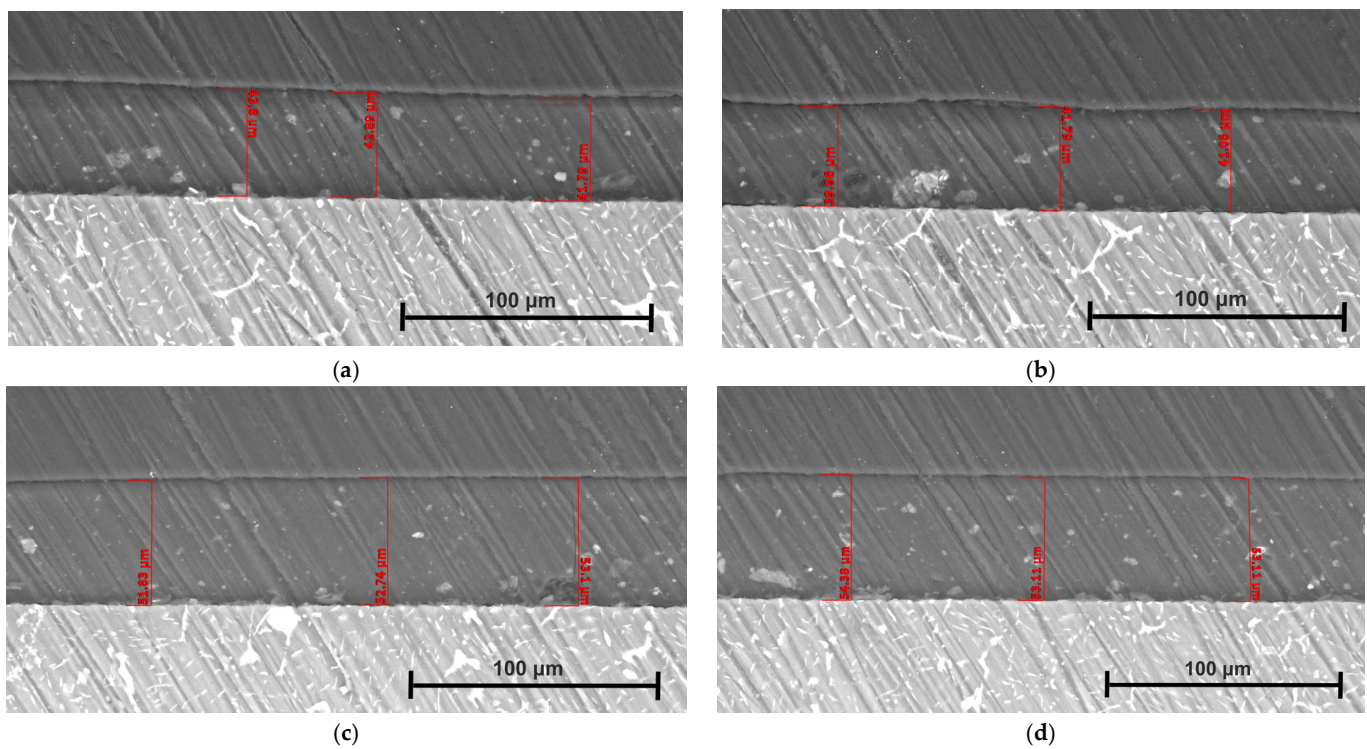


**Figure 11.** Coating thickness deposited on the Mg3Nd alloy surfaces: (a) Mg3Nd\_A\_CAHAp; (b) Mg3Nd\_A\_CAMg; (c) Mg3Nd\_B\_CAHAp; (d) Mg3Nd\_B\_CAMg.

### 3.2. Corrosion Behavior of the Experimental Samples

#### 3.2.1. Immersion Test

The mass loss values obtained by immersing the experimental samples in the SBF solution after 72, 168, and 336 h are presented in Figure 12.

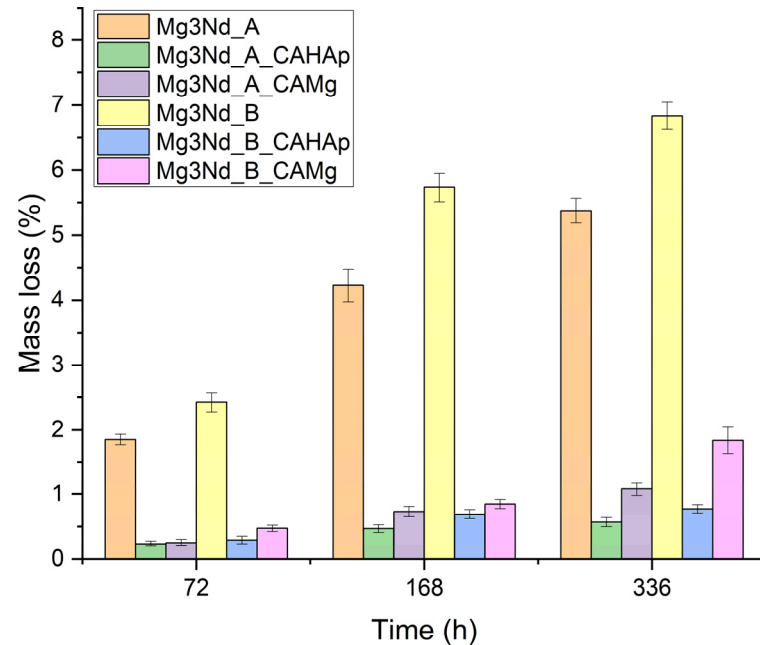
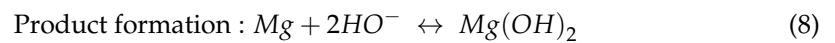
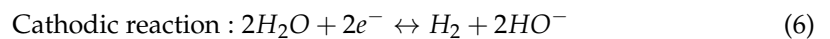
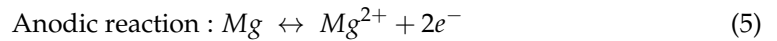
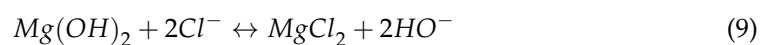


**Figure 12.** Mass loss evolution of the uncoated and coated Mg3Nd alloys in SBF solution.

The specific reactions of the magnesium and its alloy corrosion process in aqueous media produce magnesium hydroxide and hydrogen [48] according to the following reactions:



The anodic reaction takes place inside the  $\alpha$ -Mg matrix, which, due to a very negative electrode potential, is prone to be galvanically attacked. When the concentration of chlorine ions ( $\text{Cl}^{-}$ ) from the composition of the corrosion environment exceeds 30 mmol/L, the magnesium hydroxide layer will react with  $\text{Cl}^{-}$  to form magnesium chloride ( $\text{MgCl}_2$ , highly soluble) and hydroxyl ions. The concentration of chlorine ions in the physiological medium is around 150 mmol/L, which is much higher than the concentration that the magnesium hydroxide layer can support. As a result, Mg alloys will suffer severe corrosion and rapid degradation in vivo. When the  $\text{Mg}(\text{OH})_2$  layer reacts with  $\text{Cl}^{-}$  ions, it releases hydroxide ions ( $\text{OH}^{-}$ ) leading to a local increase in pH.



The lowest values were recorded for Mg-based alloys coated with composite coatings based on cellulose acetate with HAp particles (0.56% for Mg3Nd\_A\_CAHAp at 336 h and 0.77% for Mg3Nd\_B\_CAHAp at 336 h). For the uncoated alloys, the mass loss at 336 h is 5.37% for the Mg3Nd\_A alloy and 6.83% for the Mg3Nd\_B alloy. The results highlight

yttrium’s beneficial effect on the alloys’ corrosion behavior. A higher proportion of Y (2.10% in the Mg3Nd\_A alloy compared to 0.21% in the Mg3Nd\_B alloy) generates a lower mass loss and, therefore, a higher corrosion resistance due to the alloy microstructure’s refinement. For the uncoated alloys (Mg3Nd\_A and Mg3Nd\_B), a higher mass loss is observed during the first 168 h of immersion. After this time, the corrosion process is reduced in intensity due to the increase in pH to a value at which the Mg(OH)<sub>2</sub> layer is stable on the surface of the magnesium alloys. Also, the results reveal that the composite coatings made on the Mg3Nd alloy surface provide protection against the test environment. The results obtained for the Mg3Nd\_A\_CAHAp and Mg3Nd\_B\_CAHAp samples are 10 and 9 times lower than the uncoated alloys, respectively, and for the Mg3Nd\_A\_CAMg and Mg3Nd\_B\_CAMg samples, 5 and 4 times lower than the uncoated alloys.

The results showed that, in the case of both Mg3Nd alloys, the composite coating based on CA with HAP particles achieves the best protection against the test environment.

### 3.2.2. Electrochemical Tests

The Tafel curves for coated and uncoated samples are presented in Figure 13.

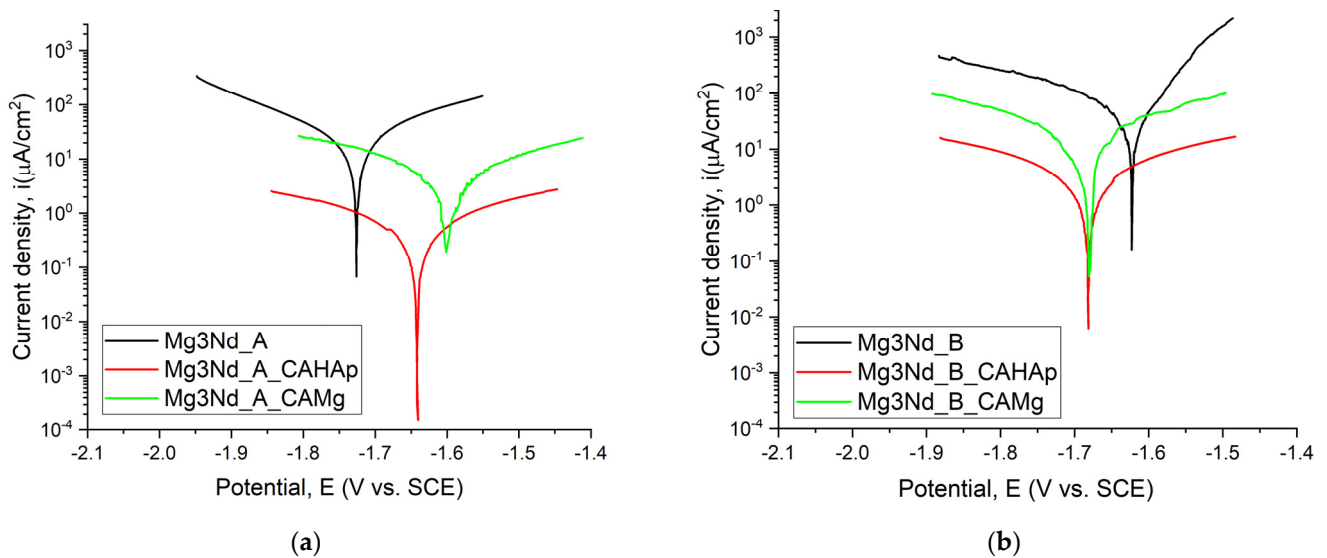


Figure 13. Tafel variations of the uncoated and coated samples: (a) Mg3Nd\_A; (b) Mg3Nd\_B.

The electrochemical measurements for the uncoated and coated alloys are presented in Table 3.

Table 3. The electrochemical parameters obtained on the coated and uncoated Mg3Nd alloys.

Sample ID	$E_{oc}$ (V)	$E_{corr}$ (V)	$i_{corr}$ ( $\mu\text{A}/\text{cm}^2$ )	$\beta_c$ (mV)	$\beta_a$ (mV)	CR (mm/Year)	$P_e$ (%)	$R_p$ ( $\text{k}\Omega\text{cm}^2$ )
Mg3Nd_A	−1.765	−1.720	38.918	266.60	280.011	0.885	-	1.530
Mg3Nd_A_CAHAp	−1.647	−1.641	4.497	2637	1371	-	99.63	87.210
Mg3Nd_A_CAMg	−1.610	−1.605	16.684	625.154	676.912	-	98.66	8.469
Mg3Nd_B	−1.698	−1.629	55.689	268.870	87.419	1.266	-	0.535
Mg3Nd_B_CAHAp	−1.683	−1.681	14.971	1008	788.346	-	98.54	12.847
Mg3Nd_B_CAMg	−1.696	−1.678	20.607	297.275	242.764	-	97.99	2.819

The corrosion resistance of the uncoated and coated Mg3Nd samples was analyzed based on different evaluation criteria. It is well known that a more electropositive value of the open circuit potential ( $E_{oc}$ ) is directly linked to a nobler character from an electrochemical point of view and a much better corrosion behavior in SBF. By analyzing the values presented in Table 3, it can be noticed that all the coated samples exhibited better

corrosion resistance than uncoated alloys. The much more electropositive values of  $E_{oc}$  were obtained for Mg3Nd\_A\_CAMg (−1.610 V) and Mg3Nd\_A\_CAHAp (−1.647 V) at a difference of only 0.37 V. Also, the Mg3Nd\_B\_CAMg (−1.696 V) and Mg3Nd\_B\_CAHAp (−1.683 V) were characterized by good corrosion behavior. If we consider the corrosion potential criteria ( $E_{corr}$ ), the more electropositive values are obtained for the coated samples, which are ranked as follows: Mg3Nd\_A\_CAMg (−1.605 V), Mg3Nd\_A\_CAHAp (−1.641 V), Mg3Nd\_B\_CAMg (−1.678 V), and Mg3Nd\_B\_CAHAp (−1.681 V).

Regarding the corrosion current density, the smallest value shows a higher corrosion resistance. In our case, the lowest value of  $i_{corr}$  was achieved for the samples with a composite coating based on CA and HAp particles (i.e., Mg3Nd\_A\_CAHAp−4.497  $\mu\text{A}/\text{cm}^2$ , Mg3Nd\_B\_CAHAp−14.971  $\mu\text{A}/\text{cm}^2$ ). Also, a good corrosion behavior was noticed for the samples coated with composite coatings based on CA and Mg particles, but the values of the corrosion current density were higher than those previously mentioned (Mg3Nd\_A\_CAMg−16.684  $\mu\text{A}/\text{cm}^2$ , Mg3Nd\_B\_CAMg−20.607  $\mu\text{A}/\text{cm}^2$ ). It can be concluded that both composite coatings offered very high protection against corrosion. From the polarization resistance ( $R_p$ ) point of view, a higher value of this parameter indicates an increased corrosion resistance. The electrochemical tests made in SBF showed that Mg3Nd\_A\_CAHAp (87.210  $\text{k}\Omega\text{cm}^2$ ) and Mg3Nd\_B\_CAHAp (12.847  $\text{k}\Omega\text{cm}^2$ ) exhibited the best corrosion behavior. The composite coating based on CA and Mg particles offered medium protection against corrosion (Mg3Nd\_A\_CAMg−8.469  $\text{k}\Omega\text{cm}^2$ , Mg3Nd\_B\_CAMg−2.819  $\text{k}\Omega\text{cm}^2$ ) in comparison with the uncoated samples that exhibited the lowest value of the polarization resistance (Mg3Nd\_A−1.530  $\text{k}\Omega\text{cm}^2$ , Mg3Nd\_B−0.535  $\text{k}\Omega\text{cm}^2$ ). The corrosion rate can be computed only in the case of uncoated samples, and it can be seen that the Mg3Nd\_A had a lower value (0.885 mm/year) than Mg3Nd\_B (1.266 mm/year). The protective efficiency must have a higher value to indicate the protective effect of the coating against the corrosion phenomenon. This parameter can be computed only in the case of coated samples. It can be noticed that the best protective efficiency is offered by composite coatings based on CA with HAp or Mg in the case of the Mg3Nd\_A alloy. The same order is observed for the Mg3Nd\_B material, but the protective efficiency had lower values.

Gaon et al. [49] investigated the effect of the local microstructure of Mg-Zr-Nd-Y-based alloys on their corrosion behavior compared with other magnesium-based alloys. A skin effect was noticed for the higher Y content alloy during the corrosion process due to the higher content of Mg3Nd phase. The authors found a correlation between the grain structure and corrosion rate and stated that a coarser grain determined an increased corrosion rate. They found that the mass loss ( $P_w$ ) for the Mg-Zr-Nd-Y-based alloy with Y higher content was about  $1.46 \pm 0.04$  mm/year and a gas evolution ( $P_H$ ) of about  $1.29 \pm 0.06$  mm/year, while for the Mg-Zr-Nd-Y-based alloy with a lower Y content,  $P_w$  was equal to  $6.21 \pm 0.05$  mm/year and pH was  $7.73 \pm 0.05$ . It can be observed that an increased Y content generated a higher corrosion resistance.

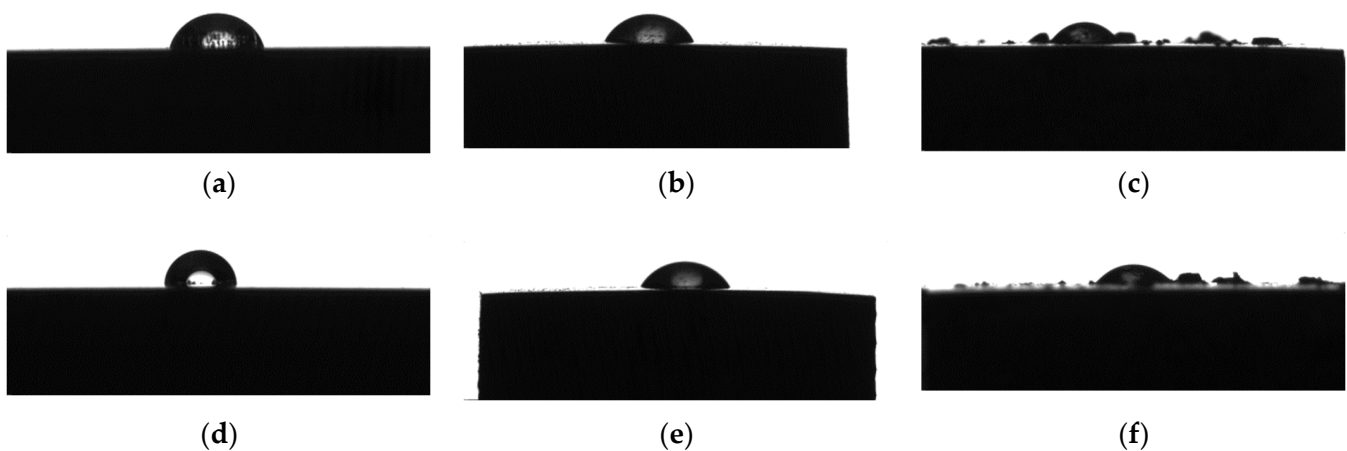
Zemkova et al. [50] analyzed the effect of rare earth addition on the corrosion behavior of Mg3Nd (N3), Mg-3Y (W3), and Mg-4Y-3Nd (WN43). They noticed that Mg-Y secondary phase particles had a detrimental effect on the corrosion process by reducing the value of the corrosion resistance [51,52], since for the case in which Y is dissolved in the magnesium matrix, the corrosion resistance increased [53]. Regarding the WN43 alloy, the second phase Mg- (Nd, Y) did not generate a severe galvanic corrosion effect because the potential difference between the secondary phase and  $\alpha$ -Mg matrix is only about 25 mV [54].

As a final observation from the protective effect of the coating, the best protective efficiency for both the Mg3Nd alloys is offered by the composite coating based on CA with HAp particles. The composite coating based on CA with Mg particles was also efficient but less than the coating mentioned before. The two developed films determined increased corrosion resistance and have great potential to be used as coatings for Mg-based implants.

### 3.3. Surface Properties of the Experimental Samples

#### 3.3.1. Wettability

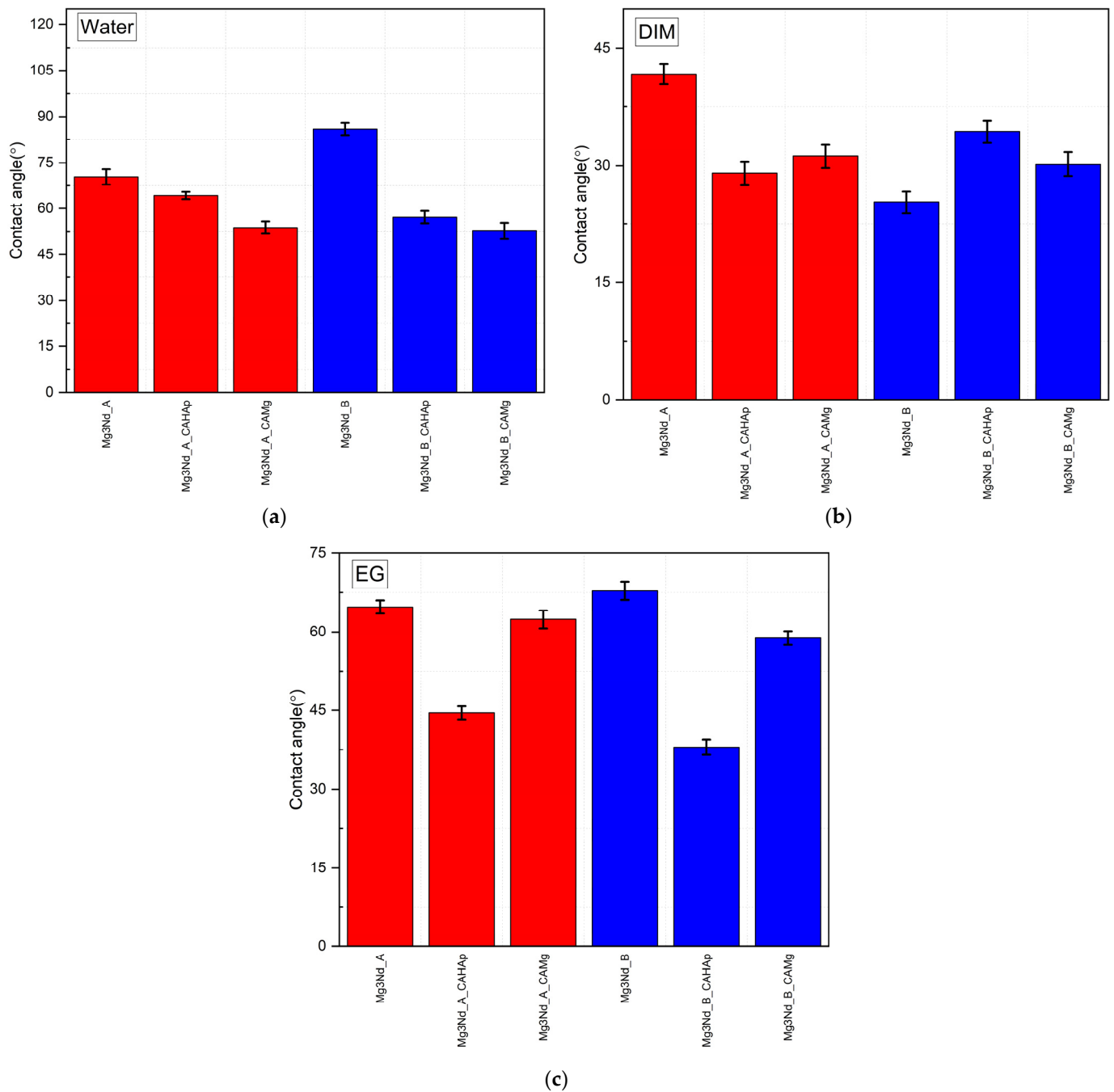
The wettability investigation is important to establish if the material surface represents a proper medium for an adequate biological response. It is well known that in the case of high hydrophilicity, cell proliferation and adhesion increase, and a better osteointegration of the implant occurs. Higher than  $90^\circ$  contact angles characterize a hydrophobic surface, which sometimes is not favorable to protein and molecule absorption from the biological fluids. Figure 14 presents examples of droplets for the Mg3Nd\_A and Mg3Nd\_B alloys in the case of water as a wetting agent for control (uncoated sample) and coated samples. It can be observed that in the case of Mg3Nd\_A and Mg3Nd\_B alloys, the composite coatings based on CA reinforced with HAp or Mg particles transform the alloy surface into a more hydrophilic one, with the lowest value of contact angle ( $52.79^\circ$ ) obtained for the Mg3Nd\_B\_CAMg.



**Figure 14.** Examples of droplet shape and average values obtained for the experimental samples. For Mg3Nd\_A: (a) control sample ( $70.37 \pm 2.52^\circ$ ); (b) Mg3Nd\_A\_CAHAp ( $64.23 \pm 1.19^\circ$ ); (c) Mg3Nd\_A\_CAMg ( $53.89 \pm 1.98^\circ$ ); for Mg3Nd\_B; (d) control sample ( $85.91 \pm 2.02^\circ$ ); (e) Mg3Nd\_B\_CAHAp ( $57.21 \pm 1.95^\circ$ ); (f) Mg3Nd\_B\_CAMg ( $52.79 \pm 2.62^\circ$ ). Wetting agent–water.

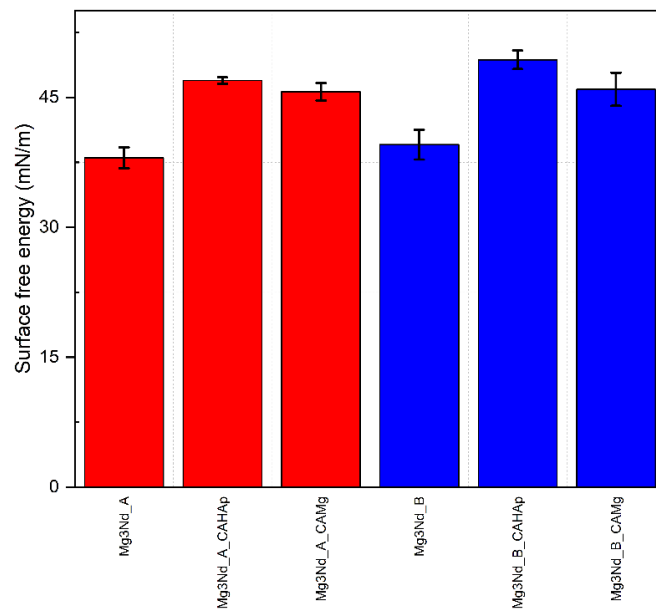
The HAp particles included in the composite coating determine the hydrophilic behavior of the surface with a contact angle of about  $57.21^\circ$  (Mg3Nd\_B\_CAHAp) and  $64.23^\circ$  (Mg3Nd\_A\_CAHAp). It can be concluded that the coating procedure in the case of both the Mg-REs alloys is directly linked to hydrophilization of the surface with a much more predominant effect in the case of Mg3Nd\_B alloy.

Figure 15 shows the graphs for the tested samples obtained in the case of the three wetting agents. For the diiodomethane liquid, the Mg3Nd\_A\_CAHAp and Mg3Nd\_B exhibited the most hydrophilic characters, with a contact angle of about  $29 \pm 1.49^\circ$  and  $25.3 \pm 1.4^\circ$ . In the case of the ethylene glycol wetting agent, the samples with a composite coating based on CA with HAp particles have the lowest contact angle value (i.e., Mg3Nd\_A\_CAHAp– $44.53^\circ$ , Mg3Nd\_B\_CAHAp– $37.99^\circ$ ).



**Figure 15.** Contact angles (average values and standard deviations) for the Mg-REs alloys for three wetting agents: (a) water; (b) diiodomethane; (c) ethylene glycol.

Based on the fact that ethylene glycol (EG) and water (W) are considered polar liquids, while diiodomethane (DIM) is a nonpolar/dispersive liquid, and their surface energy components are known as reported in [41], in Figure 16 the alloy surface free energy (SFE) is shown after the OWKR method was applied. The surface wettability can be directly correlated with SFE. Higher energy values are usually associated with lower values of contact angles and are characteristic of a surface with increased cell proliferation properties and absorption of biological substances [55–59]. The cell behavior could be predicted more accurately just after a complex surface characterization, including chemical composition, topography, roughness, and wettability.



**Figure 16.** Surface free energy (SFE) results of the investigated samples computed with OWKR method.

In our case, the samples coated with composite coatings based on CA with HAP particles exhibited the highest value of SFE, since the lowest values characterized the uncoated samples.

The work of adhesion represents the reversible thermodynamic work, which is necessary to separate the interface in an equilibrium state between two phases if an infinite distance is considered. The obtained values are presented in Figure 17 for water as a wetting agent. An increased interfacial attraction determines a high work of adhesion value. In the case of Mg3Nd\_A alloy, a value of  $91.4 \pm 2.58 \text{ mJ/m}^2$  was obtained. After the composite coatings based on CA with HAP or Mg particles were applied, the work of adhesion increased to  $100.36 \pm 1.18 \text{ mJ/m}^2$  and  $107.13 \text{ mJ/m}^2$ , respectively. For the Mg3Nd\_B alloy, the work of adhesion increased from  $73.31 \pm 1.77 \text{ mJ/m}^2$  to  $108.22 \pm 0.98 \text{ mJ/m}^2$  (Mg3Nd\_B\_CAHAp sample) and  $112.28 \pm 1.24 \text{ mJ/m}^2$  (Mg3Nd\_B\_CAMg sample).

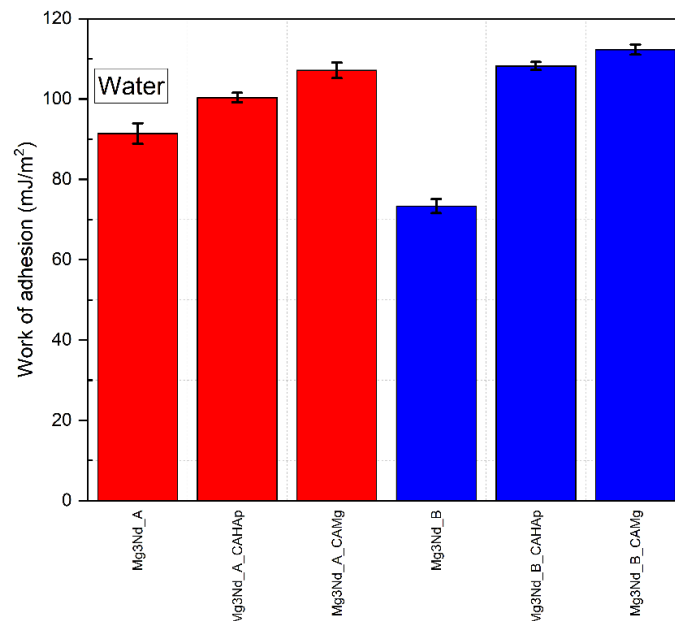


**Figure 17.** Work of adhesion in the case of water as the wetting agent for the tested samples.

From the contact angle analyses, it can be concluded that the samples with a composite coating based on CA with HAp are the most beneficial to cell adhesion and proliferation and adequate for increased osteogenesis. Our analysis can be considered in good accordance with the literature. In the case of the Mg-Zn-Y-Nd alloy used as potential material for biodegradable stent manufacture, Wang et al. [60] obtained a contact angle of about  $60^\circ$ . Indira et al. [61] studied the wettability properties of laser surface-modified rare earth Mg alloys. They used the commercial Mg4Y3Nd0.5Zr (WE43) alloy in their studies and measured a contact angle for the control sample of  $81^\circ$  and  $61^\circ$  for deionized water and SBF as wetting agents. Their main conclusion was that the laser surface treatment modified the surface character by transforming it into a more hydrophilic one (i.e., a contact angle of  $43^\circ$  was obtained for deionized water). The small differences between our results and those found in the literature can be attributed to the different materials' chemical compositions and concentrations of rare earths.

The results regarding the contact angle measurements were compared using one-way ANOVA assuming equal variances with a confidence level of 95% associated with Tukey and Fisher's simultaneous tests of the means. It can be concluded, at  $\alpha = 0.05$ , that the means are significantly different—the surface modification is an influence factor for wetting behavior. The Tukey and Fisher tests yielded that through groups, some means can be considered equal, an aspect that was expected given the same nature of the coating. The differences between the means for the coatings can be attributed to the roughness and dispersion of the HAp and Mg particles, easily observed in the averages of the surface free energy: a significant increase post-coating and small differences between coated samples. The main contribution in surface-free energy can be attributed to the matrix of the coating, while the reinforcing phase shows a milder one.

### 3.3.2. Roughness

The surface roughness is an important parameter that should be taken into consideration when implant integration in the human body is necessary. The literature revealed that roughness had a direct influence on the material degradation rate [62–64], cell adhesion and proliferation [65,66], and osteointegration [67,68]. Some research showed that a rough surface had a beneficial effect in the reduction in the degradation rate [69–72], since other investigations sustained the contrary [66,73]. The surface topography was investigated based on profilometry analysis. Our results revealed that the uncoated samples had the lowest values of the  $R_a$  and  $R_q$  parameters (e.g., Mg3Nd\_A:  $R_a = 0.996 \pm 0.021 \mu\text{m}$ ,  $R_q = 0.208 \pm 0.023 \mu\text{m}$ ; Mg3Nd\_B:  $R_a = 0.218 \pm 0.022 \mu\text{m}$ ,  $R_q = 0.284 \pm 0.026 \mu\text{m}$ ). In the case of the first alloy (Mg3Nd\_A), the composite coating based on CA with Mg particles generated a higher increase in the  $R_q$  parameter ( $R_q = 2.87 \pm 0.030 \mu\text{m}$ ) in comparison with the sample with composite coatings based on CA and HAp particles ( $R_q = 1.94 \pm 0.033 \mu\text{m}$ ), since regarding the  $R_a$  parameter, similar values of about  $1.222 \pm 0.032 \mu\text{m}$  (Mg3Nd\_A\_CAMg) and  $1.024 \pm 0.034 \mu\text{m}$  (Mg3Nd\_A\_CAHAp) were achieved. For the second investigated alloy (Mg3Nd\_B), the highest values of the roughness parameters were obtained in the case of composite coating based on CA with Mg particles ( $R_a = 1.288 \pm 0.050 \mu\text{m}$ ,  $R_q = 3.310 \pm 0.057 \mu\text{m}$ ), followed by composite coating based on CA with HAp particles ( $R_a = 0.933 \pm 0.022 \mu\text{m}$ ,  $R_q = 1.304 \pm 0.042 \mu\text{m}$ ) (Figure 18).

A correlation between surface roughness and wettability was given in the literature by the Wenzel model [74]. This theory states that an increase in the roughness will determine a decrease in the contact angle in the case of hydrophilic surfaces. This observation is valid in our case for both alloys and water as a wetting agent, correlating to an increase in the roughness surface due to coating procedures with a more hydrophilic surface (Figure 15a). A similar one-way ANOVA was performed on the roughness results, yielding that the mean values are different; the Tukey and Fisher tests suggest that the only means that can be considered equal for  $R_a$  are those of Mg3Nd\_A and Mg3Nd\_A\_CAHAp.

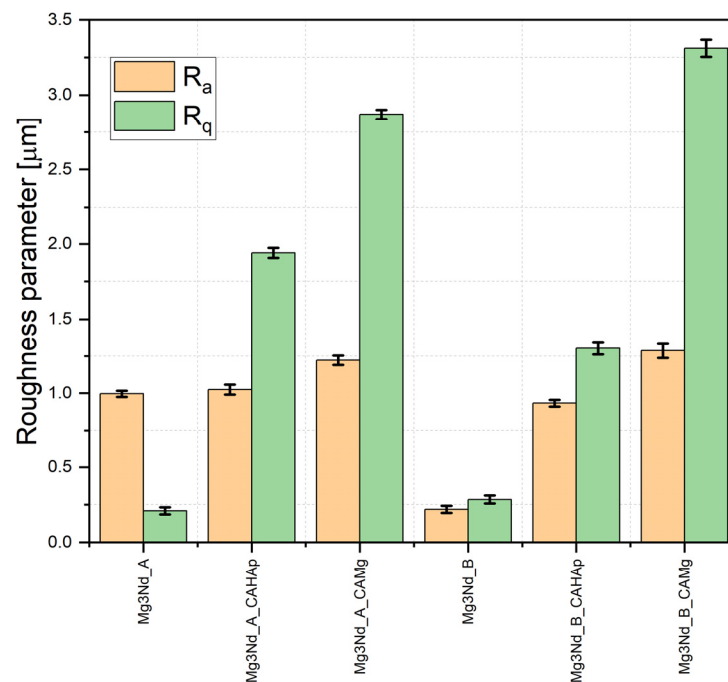


**Figure 18.**  $R_a$  and  $R_q$  parameters for surface roughness of the investigated alloys.

#### 4. Conclusions

The present study investigated the effect of CA-based composite coatings reinforced with hydroxyapatite or magnesium particles applied on the two Mg3Nd alloys on their surface properties and corrosion behavior. The SEM images revealed the presence of homogenous coating layers in both the coatings, which ensure a high protective behavior against the corrosion process. In addition, the CA-based composite coatings determined a decrease in contact angle and an increase in roughness values, a fact that evidences the existence of an environment that is favorable for the promotion of cell growth, proliferation, and adhesion.

The in vitro research highlighted that the composite coating based on CA with HAp particles exhibited the best functional properties for both of the investigated Mg3Nd alloys. The composite coating based on CA with Mg particles was also efficient but in a reduced amount. Considering the results presented in this study, we can conclude that the proposed CA-based composite coatings have great potential to be used in coated Mg alloy implant manufacture.

**Author Contributions:** Conceptualization, A.S., I.A. and J.V.R.; methodology, I.A., V.M. and A.A.; software, R.C. and H.D.; validation, I.A., J.V.R. and M.F.; formal analysis, V.M., M.F. and H.D.; investigation, A.S., R.C., A.A., C.-M.C., M.M. and F.M.; resources, I.A. and J.V.R.; data curation, I.A., V.M., A.A. and J.V.R.; writing—original draft preparation, A.S., M.F., A.A. and V.M.; writing—review and editing, A.S., M.F. and A.A.; visualization, M.F. and H.D.; supervision, I.A.; project administration, I.A. and J.V.R.; funding acquisition, I.A. All authors have read and agreed to the published version of the manuscript.

**Funding:** This work was supported by a grant of the Romanian Ministry of Education and Research, CNCS-UEFISCDI, project number PN-III-P4-ID-PCE-2020-2591, within PNCDI III. In addition, this work was supported by a grant from the National Program for Research of the National Association of Technical Universities—GNAC ARUT 2023 (Project number 29/9.10.2023, Project ID 220235050).

**Institutional Review Board Statement:** Not applicable.

**Data Availability Statement:** Data are contained within the article.

**Conflicts of Interest:** The authors declare no conflict of interest.

## References

1. Prasad, S.V.S.; Prasad, S.B.; Verma, K.; Mishra, R.K.; Kumar, V.; Singh, S. The Role and Significance of Magnesium in Modern Day Research—A Review. *J. Magnes. Alloys* **2022**, *10*, 1–61. [[CrossRef](#)]
2. Antoniac, I.; Miculescu, M.; Mănescu, V.; Stere, A.; Quan, P.H.; Păltânea, G.; Robu, A.; Earar, K. Magnesium-Based Alloys Used in Orthopedic Surgery. *Materials* **2022**, *15*, 1148. [[CrossRef](#)] [[PubMed](#)]
3. Antoniac, I.V.; Filipescu, M.; Barbaro, K.; Bonciu, A.; Birjega, R.; Cotrut, C.M.; Galvano, E.; Fosca, M.; Fadeeva, I.V.; Vadalà, G.; et al. Iron Ion-Doped Tricalcium Phosphate Coatings Improve the Properties of Biodegradable Magnesium Alloys for Biomedical Implant Application. *Adv. Mater. Interfaces* **2020**, *7*, 2000531. [[CrossRef](#)]
4. Xing, F.; Li, S.; Yin, D.; Xie, J.; Rommens, P.M.; Xiang, Z.; Liu, M.; Ritz, U. Recent Progress in Mg-Based Alloys as a Novel Bioabsorbable Biomaterials for Orthopedic Applications. *J. Magnes. Alloys* **2022**, *10*, 1428–1456. [[CrossRef](#)]
5. Zeng, Z.; Salehi, M.; Kopp, A.; Xu, S.; Esmaily, M.; Birbilis, N. Recent Progress and Perspectives in Additive Manufacturing of Magnesium Alloys. *J. Magnes. Alloys* **2022**, *10*, 1511–1541. [[CrossRef](#)]
6. Uppal, G.; Thakur, A.; Chauhan, A.; Bala, S. Magnesium Based Implants for Functional Bone Tissue Regeneration—A Review. *J. Magnes. Alloys* **2022**, *10*, 356–386. [[CrossRef](#)]
7. Sekar, P.S.N.; Desai, V. Recent Progress in in Vivo Studies and Clinical Applications of Magnesium Based Biodegradable Implants—A Review. *J. Magnes. Alloys* **2021**, *9*, 1147–1163. [[CrossRef](#)]
8. Sahu, M.R.; Kumar, T.S.S.; Chakkingal, U. A Review on Recent Advancements in Biodegradable Mg-Ca Alloys. *J. Magnes. Alloys* **2022**, *10*, 2094–2117. [[CrossRef](#)]
9. Atrens, A.; Song, G.-L.; Cao, F.; Shi, Z.; Bowen, P.K. Advances in Mg Corrosion and Research Suggestions. *J. Magnes. Alloys* **2013**, *1*, 177–200. [[CrossRef](#)]
10. Bamberger, M.; Dehm, G. Trends in the Development of New Mg Alloys. *Annu. Rev. Mater. Res.* **2008**, *38*, 505–533. [[CrossRef](#)]
11. Blawert, C.; Fechner, D.; Höche, D.; Heitmann, V.; Dietzel, W.; Kainer, K.U.; Živanović, P.; Scharf, C.; Ditzel, A.; Gröbner, J.; et al. Magnesium Secondary Alloys: Alloy Design for Magnesium Alloys with Improved Tolerance Limits against Impurities. *Corros. Sci.* **2010**, *52*, 2452–2468. [[CrossRef](#)]
12. Han, L.; Hu, H.; Northwood, D.O.; Li, N. Microstructure and Nano-Scale Mechanical Behavior of Mg–Al and Mg–Al–Ca Alloys. *Mater. Sci. Eng. A* **2008**, *473*, 16–27. [[CrossRef](#)]
13. Kirkland, N.T.; Staiger, M.P.; Nisbet, D.; Davies, C.H.J.; Birbilis, N. Performance-Driven Design of Biocompatible Mg Alloys. *JOM* **2011**, *63*, 28–34. [[CrossRef](#)]
14. Radha, R.; Sreekanth, D. Insight of Magnesium Alloys and Composites for Orthopedic Implant Applications—A Review. *J. Magnes. Alloys* **2017**, *5*, 286–312. [[CrossRef](#)]
15. Bairagi, D.; Mandal, S. A Comprehensive Review on Biocompatible Mg-Based Alloys as Temporary Orthopaedic Implants: Current Status, Challenges, and Future Prospects. *J. Magnes. Alloys* **2022**, *10*, 627–669. [[CrossRef](#)]
16. Sun, J.; Du, W.; Fu, J.; Liu, K.; Li, S.; Wang, Z.; Liang, H. A Review on Magnesium Alloys for Application of Degradable Fracturing Tools. *J. Magnes. Alloys* **2022**, *10*, 2649–2672. [[CrossRef](#)]
17. Neil, W.C.; Forsyth, M.; Howlett, P.C.; Hutchinson, C.R.; Hinton, B.R.W. Corrosion of Heat Treated Magnesium Alloy ZE41. *Corros. Sci.* **2011**, *53*, 3299–3308. [[CrossRef](#)]
18. Loos, A.; Rohde, R.; Haverich, A.; Barlach, S. In Vitro and In Vivo Biocompatibility Testing of Absorbable Metal Stents. *Macromol. Symp.* **2007**, *253*, 103–108. [[CrossRef](#)]
19. Chang, J.; Guo, X.; He, S.; Fu, P.; Peng, L.; Ding, W. Investigation of the Corrosion for Mg–XGd–3Y–0.4Zr (X = 6, 8, 10, 12 wt%) Alloys in a Peak-Aged Condition. *Corros. Sci.* **2008**, *50*, 166–177. [[CrossRef](#)]
20. Darrach, T.H.; Prutsman-Pfeiffer, J.J.; Poreda, R.J.; Ellen Campbell, M.; Hauschka, P.V.; Hannigan, R.E. Incorporation of Excess Gadolinium into Human Bone from Medical Contrast Agents. *Metallomics* **2009**, *1*, 479. [[CrossRef](#)]
21. Wu, A.; Xia, C. Study of the Microstructure and Mechanical Properties of Mg–Rare Earth Alloys. *Mater. Des.* **2007**, *28*, 1963–1967. [[CrossRef](#)]
22. Kawagoe, M.; Hirasawa, F.; Cun Wang, S.; Liu, Y.; Ueno, Y.; Sugiyama, T. Orally Administrated Rare Earth Element Cerium Induces Metallothionein Synthesis and Increases Glutathione in the Mouse Liver. *Life Sci.* **2005**, *77*, 922–937. [[CrossRef](#)]
23. Willbold, E.; Gu, X.; Albert, D.; Kalla, K.; Bobe, K.; Brauneis, M.; Janning, C.; Nellesen, J.; Czayka, W.; Tillmann, W.; et al. Effect of the Addition of Low Rare Earth Elements (Lanthanum, Neodymium, Cerium) on the Biodegradation and Biocompatibility of Magnesium. *Acta Biomater.* **2015**, *11*, 554–562. [[CrossRef](#)]
24. He, F.; Hu, W.; Liu, L.; Ma, S.; He, W. Effect of Zn Addition on Microstructure and Mechanical Properties of Mg–3Y–2Nd–0.5Zr Alloy. *China Foundry* **2023**, *20*, 299–306. [[CrossRef](#)]
25. Chen, Y.; Wu, G.; Liu, W.; Zhang, L.; Zhang, H.; Cui, W. Effects of Minor Y Addition on Microstructure and Mechanical Properties of Mg–Nd–Zn–Zr Alloy. *J. Mater. Res.* **2017**, *32*, 3712–3722. [[CrossRef](#)]
26. Tian, K.V.; Passaretti, F.; Nespoli, A.; Placidi, E.; Condò, R.; Andreani, C.; Licoccia, S.; Chass, G.A.; Senesi, R.; Cozza, P. Composition—Nanostructure Steered Performance Predictions in Steel Wires. *Nanomaterials* **2019**, *9*, 1119. [[CrossRef](#)] [[PubMed](#)]
27. Kirkland, N.T.; Lespagnol, J.; Birbilis, N.; Staiger, M.P. A Survey of Bio-Corrosion Rates of Magnesium Alloys. *Corros. Sci.* **2010**, *52*, 287–291. [[CrossRef](#)]

28. Rau, J.V.; Antoniac, I.; Filipescu, M.; Cotrut, C.; Fosca, M.; Nistor, L.C.; Birjega, R.; Dinescu, M. Hydroxyapatite Coatings on Mg–Ca Alloy Prepared by Pulsed Laser Deposition: Properties and Corrosion Resistance in Simulated Body Fluid. *Ceram. Int.* **2018**, *44*, 16678–16687. [[CrossRef](#)]
29. Antoniac, I.; Miculescu, F.; Cotrut, C.; Ficai, A.; Rau, J.V.; Grosu, E.; Antoniac, A.; Tecu, C.; Cristescu, I. Controlling the Degradation Rate of Biodegradable Mg–Zn–Mn Alloys for Orthopedic Applications by Electrophoretic Deposition of Hydroxyapatite Coating. *Materials* **2020**, *13*, 263. [[CrossRef](#)]
30. Quan, P.H.; Antoniac, I.; Miculescu, F.; Antoniac, A.; Manescu, V.; Robu, A.; Bița, A.I.; Miculescu, M.; Saceleanu, A.; Bodog, A.D.; et al. Fluoride Treatment and In Vitro Corrosion Behavior of Mg–Nd–Y–Zn–Zr Alloys Type. *Materials* **2022**, *15*, 566. [[CrossRef](#)]
31. Saberi, A.; Bakhsheshi-Rad, H.R.; Abazari, S.; Ismail, A.F.; Sharif, S.; Ramakrishna, S.; Daroonparvar, M.; Berto, F. A Comprehensive Review on Surface Modifications of Biodegradable Magnesium-Based Implant Alloy: Polymer Coatings Opportunities and Challenges. *Coatings* **2021**, *11*, 747. [[CrossRef](#)]
32. Neacsu, P.; Staras, A.; Voicu, S.; Ionascu, I.; Soare, T.; Uzun, S.; Cojocaru, V.; Pandele, A.; Croitoru, S.; Miculescu, F.; et al. Characterization and In Vitro and In Vivo Assessment of a Novel Cellulose Acetate-Coated Mg-Based Alloy for Orthopedic Applications. *Materials* **2017**, *10*, 686. [[CrossRef](#)] [[PubMed](#)]
33. Alabbasi, A.; Liyanaarachchi, S.; Kannan, M.B. Polylactic Acid Coating on a Biodegradable Magnesium Alloy: An in Vitro Degradation Study by Electrochemical Impedance Spectroscopy. *Thin Solid Films* **2012**, *520*, 6841–6844. [[CrossRef](#)]
34. Shi, P.; Niu, B.E.S.; Chen, Y.; Li, Q. Preparation and Characterization of PLA Coating and PLA/MAO Composite Coatings on AZ31 Magnesium Alloy for Improvement of Corrosion Resistance. *Surf. Coat. Technol.* **2015**, *262*, 26–32. [[CrossRef](#)]
35. Yazdimamaghani, M.; Razavi, M.; Vashae, D.; Tayebi, L. Development and Degradation Behavior of Magnesium Scaffolds Coated with Polycaprolactone for Bone Tissue Engineering. *Mater. Lett.* **2014**, *132*, 106–110. [[CrossRef](#)]
36. Li, J.N.; Cao, P.; Zhang, X.N.; Zhang, S.X.; He, Y.H. In Vitro Degradation and Cell Attachment of a PLGA Coated Biodegradable Mg–6Zn Based Alloy. *J. Mater. Sci.* **2010**, *45*, 6038–6045. [[CrossRef](#)]
37. Chen, L.; Sheng, Y.; Zhou, H.; Li, Z.; Wang, X.; Li, W. Influence of a MAO + PLGA Coating on Biocorrosion and Stress Corrosion Cracking Behavior of a Magnesium Alloy in a Physiological Environment. *Corros. Sci.* **2019**, *148*, 134–143. [[CrossRef](#)]
38. Streza, A.; Antoniac, A.; Manescu, V.; Paltanea, G.; Robu, A.; Dura, H.; Verestiuc, L.; Stanica, E.; Voicu, S.I.; Antoniac, I.; et al. Effect of Filler Types on Cellulose-Acetate-Based Composite Used as Coatings for Biodegradable Magnesium Implants for Trauma. *Materials* **2023**, *16*, 554. [[CrossRef](#)] [[PubMed](#)]
39. Bița, A.-I.; Antoniac, I.; Miculescu, M.; Stan, G.E.; Leonat, L.; Antoniac, A.; Constantin, B.; Forna, N. Electrochemical and In Vitro Biological Evaluation of Bio-Active Coatings Deposited by Magnetron Sputtering onto Biocompatible Mg-0.8Ca Alloy. *Materials* **2022**, *15*, 3100. [[CrossRef](#)]
40. Kokubo, T.; Takadama, H. How Useful Is SBF in Predicting in Vivo Bone Bioactivity? *Biomaterials* **2006**, *27*, 2907–2915. [[CrossRef](#)] [[PubMed](#)]
41. Annamalai, M.; Gopinadhan, K.; Han, S.A.; Saha, S.; Park, H.J.; Cho, E.B.; Kumar, B.; Patra, A.; Kim, S.-W.; Venkatesan, T. Surface Energy and Wettability of van Der Waals Structures. *Nanoscale* **2016**, *8*, 5764–5770. [[CrossRef](#)]
42. Xu, D.K.; Liu, L.; Xu, Y.B.; Han, E.H. The Influence of Element Y on the Mechanical Properties of the As-Extruded Mg–Zn–Y–Zr Alloys. *J. Alloys Compd.* **2006**, *426*, 155–161. [[CrossRef](#)]
43. Wang, J.; Liu, R.; Dong, X.; Yang, Y. Microstructure and Mechanical Properties of Mg–Zn–Y–Nd–Zr Alloys. *J. Rare Earths* **2013**, *31*, 616–621. [[CrossRef](#)]
44. Zhou, H.T.; Zhang, Z.D.; Liu, C.M.; Wang, Q.W. Effect of Nd and Y on the Microstructure and Mechanical Properties of ZK60 Alloy. *Mater. Sci. Eng. A* **2007**, *445–446*, 1–6. [[CrossRef](#)]
45. Zengin, H.; Turen, Y. Effect of Y Addition on Microstructure and Corrosion Behavior of Extruded Mg–Zn–Nd–Zr Alloy. *J. Magnes. Alloys* **2020**, *8*, 640–653. [[CrossRef](#)]
46. Elkaiam, L.; Hakimi, O.; Goldman, J.; Aghion, E. The Effect of Nd on Mechanical Properties and Corrosion Performance of Biodegradable Mg-5%Zn Alloy. *Metals* **2018**, *8*, 438. [[CrossRef](#)]
47. Li, Q.; Wang, Q.; Wang, Y.; Zeng, X.; Ding, W. Effect of Nd and Y Addition on Microstructure and Mechanical Properties of As-Cast Mg–Zn–Zr Alloy. *J. Alloys Compd.* **2007**, *427*, 115–123. [[CrossRef](#)]
48. Xu, L.; Liu, X.; Sun, K.; Fu, R.; Wang, G. Corrosion Behavior in Magnesium-Based Alloys for Biomedical Applications. *Materials* **2022**, *15*, 2613. [[CrossRef](#)]
49. Gaon, O.; Dror, G.; Davidi, O.; Lugovskoy, A. The Effect of the Local Microstructure of MRI 201S Magnesium Alloy on Its Corrosion Rate. *Corros. Sci.* **2015**, *93*, 167–171. [[CrossRef](#)]
50. Zemková, M.; Minárik, P.; Dittrich, J.; Bohlen, J.; Král, R. Individual Effect of Y and Nd on the Microstructure Formation of Mg–Y–Nd Alloys Processed by Severe Plastic Deformation and Their Effect on the Subsequent Mechanical and Corrosion Properties. *J. Magnes. Alloys* **2023**, *11*, 509–521. [[CrossRef](#)]
51. Zhang, X.; Li, Y.; Zhang, K.; Wang, C.; Li, H.; Ma, M.; Zang, B. Corrosion and Electrochemical Behavior of Mg–Y Alloys in 3.5% NaCl Solution. *Trans. Nonferrous Met. Soc. China* **2013**, *23*, 1226–1236. [[CrossRef](#)]
52. Sudholz, A.D.; Gusieva, K.; Chen, X.B.; Muddle, B.C.; Gibson, M.A.; Birbilis, N. Electrochemical Behaviour and Corrosion of Mg–Y Alloys. *Corros. Sci.* **2011**, *53*, 2277–2282. [[CrossRef](#)]

53. Davenport, A.J.; Padovani, C.; Connolly, B.J.; Stevens, N.P.C.; Beale, T.A.W.; Groso, A.; Stampanoni, M. Synchrotron X-ray Microtomography Study of the Role of Y in Corrosion of Magnesium Alloy WE43. *Electrochem. Solid-State Lett.* **2007**, *10*, C5. [[CrossRef](#)]
54. Coy, A.E.; Viejo, F.; Skeldon, P.; Thompson, G.E. Susceptibility of Rare-Earth-Magnesium Alloys to Micro-Galvanic Corrosion. *Corros. Sci.* **2010**, *52*, 3896–3906. [[CrossRef](#)]
55. Wu, S.; Jang, Y.S.; Lee, M.H. Enhancement of Bone Regeneration on Calcium-Phosphate-Coated Magnesium Mesh: Using the Rat Calvarial Model. *Front. Bioeng. Biotechnol.* **2021**, *9*, 652334. [[CrossRef](#)]
56. Kim, S.; Jo, J.; Lee, S.; Kang, M.; Kim, H.; Estrin, Y.; Lee, J.; Lee, J.; Koh, Y. Hydroxyapatite-coated Magnesium Implants with Improved In Vitro and in Vivo Biocorrosion, Biocompatibility, and Bone Response. *J. Biomed. Mater. Res. A* **2014**, *102*, 429–441. [[CrossRef](#)]
57. Ishizaki, T.; Saito, N.; Takai, O. Correlation of Cell Adhesive Behaviors on Superhydrophobic, Superhydrophilic, and Micropatterned Superhydrophobic/Superhydrophilic Surfaces to Their Surface Chemistry. *Langmuir* **2010**, *26*, 8147–8154. [[CrossRef](#)] [[PubMed](#)]
58. Kim, S.-Y.; Kim, Y.-K.; Jang, Y.-S.; Park, I.-S.; Lee, S.-J.; Jeon, J.-G.; Lee, M.-H. Bioactive Effect of Alkali-Heat Treated TiO<sub>2</sub> Nanotubes by Water or Acid Treatment. *Surf. Coat. Technol.* **2016**, *303*, 256–267. [[CrossRef](#)]
59. Aronov, D.; Rosen, R.; Ron, E.Z.; Rosenman, G. Tunable Hydroxyapatite Wettability: Effect on Adhesion of Biological Molecules. *Process Biochem.* **2006**, *41*, 2367–2372. [[CrossRef](#)]
60. Wang, S.; Zhang, X.; Li, J.; Liu, C.; Guan, S. Investigation of Mg–Zn–Y–Nd Alloy for Potential Application of Biodegradable Esophageal Stent Material. *Bioact. Mater.* **2020**, *5*, 1–8. [[CrossRef](#)]
61. Indira, K.; Sylvie, C.; Zhongke, W.; Hongyu, Z. Investigation of Wettability Properties of Laser Surface Modified Rare Earth Mg Alloy. *Procedia Eng.* **2016**, *141*, 63–69. [[CrossRef](#)]
62. Lorenz, C.; Brunner, J.G.; Kollmannsberger, P.; Jaafar, L.; Fabry, B.; Virtanen, S. Effect of Surface Pre-Treatments on Biocompatibility of Magnesium. *Acta Biomater.* **2009**, *5*, 2783–2789. [[CrossRef](#)] [[PubMed](#)]
63. Walter, R.; Kannan, M.B.; He, Y.; Sandham, A. Effect of Surface Roughness on the in Vitro Degradation Behaviour of a Biodegradable Magnesium-Based Alloy. *Appl. Surf. Sci.* **2013**, *279*, 343–348. [[CrossRef](#)]
64. Laycock, N.J.; Krouse, D.P.; Hendy, S.C.; Williams, D.E. Computer Simulation of Pitting Corrosion of Stainless Steels. *Interface Mag.* **2014**, *23*, 65–71. [[CrossRef](#)]
65. Zhao, Y.; Jamesh, M.I.; Li, W.K.; Wu, G.; Wang, C.; Zheng, Y.; Yeung, K.W.K.; Chu, P.K. Enhanced Antimicrobial Properties, Cytocompatibility, and Corrosion Resistance of Plasma-Modified Biodegradable Magnesium Alloys. *Acta Biomater.* **2014**, *10*, 544–556. [[CrossRef](#)]
66. Von Der Höh, N.; Bormann, D.; Lucas, A.; Denkena, B.; Hackenbroich, C.; Meyer-Lindenberg, A. Influence of Different Surface Machining Treatments of Magnesium-Based Resorbable Implants on the Degradation Behavior in Rabbits. *Adv. Eng. Mater.* **2009**, *11*, B47–B54. [[CrossRef](#)]
67. Shetty, O.; Parekh, R.B.; Tabassum, R. Surface Modifications for Endosseous Dental Implants. *Int. J. Oral Implantol. Clin. Res.* **2012**, *3*, 116–121. [[CrossRef](#)]
68. Lacefield, W.R. Materials Characteristics of Uncoated/Ceramic-Coated Implant Materials. *Adv. Dent. Res.* **1999**, *13*, 21–26. [[CrossRef](#)]
69. Salerno, M.; Reverberi, A.; Baino, F. Nanoscale Topographical Characterization of Orbital Implant Materials. *Materials* **2018**, *11*, 660. [[CrossRef](#)]
70. Hwang, D.Y.; Kim, Y.M.; Shin, D.H. Corrosion Resistance of Plasma-Anodized AZ91 Mg Alloy in the Electrolyte with/without Potassium Fluoride. *Mater. Trans.* **2009**, *50*, 671–678. [[CrossRef](#)]
71. Yoo, B.; Shin, K.R.; Hwang, D.Y.; Lee, D.H.; Shin, D.H. Effect of Surface Roughness on Leakage Current and Corrosion Resistance of Oxide Layer on AZ91 Mg Alloy Prepared by Plasma Electrolytic Oxidation. *Appl. Surf. Sci.* **2010**, *256*, 6667–6672. [[CrossRef](#)]
72. Supplit, R.; Koch, T.; Schubert, U. Evaluation of the Anti-Corrosive Effect of Acid Pickling and Sol–Gel Coating on Magnesium AZ31 Alloy. *Corros. Sci.* **2007**, *49*, 3015–3023. [[CrossRef](#)]
73. Nguyen, T.L.; Blanquet, A.; Staiger, M.P.; Dias, G.J.; Woodfield, T.B.F. On the Role of Surface Roughness in the Corrosion of Pure Magnesium in Vitro. *J. Biomed. Mater. Res. B Appl. Biomater.* **2012**, *100B*, 1310–1318. [[CrossRef](#)]
74. Sigmund, W.M.; Hsu, S.-H. *Wenzel Model Encyclopedia of Membranes*; Drioli, E., Giorno, L., Eds.; Springer: Berlin/Heidelberg, Germany, 2015; ISBN 9783642408724.

**Disclaimer/Publisher’s Note:** The statements, opinions and data contained in all publications are solely those of the individual author(s) and contributor(s) and not of MDPI and/or the editor(s). MDPI and/or the editor(s) disclaim responsibility for any injury to people or property resulting from any ideas, methods, instructions or products referred to in the content.